The Astrophysical Journal, 945:117 (24pp), 2023 March 10 https://doi.org/10.3847/1538-4357/acba06

Spatially Resolved Stellar Populations of $0.3 < z < 6.0$ Galaxies in WHL 0137–08 and MACS 0647+70 Clusters as Revealed by JWST: How Do Galaxies Grow and Quench over Cosmic Time?

Abdurro'uf[1,2], Dan Coe[1,2,3], Intae Jung[2], Henry C. Ferguson[2], Gabriel Brammer[4,5], Kartheik G. Iyer[6,20], Larry D. Bradley[2], Pratika Dayal[7], Rogier A. Windhorst[8], Adi Zitrin[9], Ashish Kumar Meena[9], Masamune Oguri[10,11], Jose M. Diego[12], Vasily Kokorev[7], Paola Dimauro[13], Angela Adamo[14], Christopher J. Conselice[15], Brian Welch[16,17,18], Eros Vanzella[19], Tiger Yu-Yang Hsiao[1], Xinfeng Xu[1], Namrata Roy[1], and Celia R. Mulcahey[1]
[1] Center for Astrophysical Sciences, Department of Physics and Astronomy, The Johns Hopkins University, 3400 N Charles Street, Baltimore, MD 21218, USA
fabdurr1@jhu.edu
[2] Space Telescope Science Institute (STScI), 3700 San Martin Drive, Baltimore, MD 21218, USA
[3] Association of Universities for Research in Astronomy (AURA), Inc. for the European Space Agency (ESA), USA
[4] Cosmic Dawn Center (DAWN), Copenhagen, Denmark
[5] Niels Bohr Institute, University of Copenhagen, Jagtvej 128, Copenhagen, Denmark
[6] Columbia Astrophysics Laboratory, Columbia University, 550 West 120th Street, New York, NY 10027, USA
[7] Kapteyn Astronomical Institute, University of Groningen, P.O. Box 800, 9700 AV Groningen, The Netherlands
[8] School of Earth and Space Exploration, Arizona State University, Tempe, AZ 85287-1404, USA
[9] Physics Department, Ben-Gurion University of the Negev, P.O. Box 653, Be'er-Sheva 84105, Israel
[10] Center for Frontier Science, Chiba University, 1-33 Yayoi-cho, Inage-ku, Chiba 263-8522, Japan
[11] Department of Physics, Graduate School of Science, Chiba University, 1-33 Yayoi-Cho, Inage-Ku, Chiba 263-8522, Japan
[12] Instituto de Física de Cantabria (CSIC-UC). Avda. Los Castros s/n. E-39005 Santander, Spain
[13] INAF—Osservatorio Astronomico di Roma, via di Frascati 33, I-00078 Monte Porzio Catone, Italy
[14] Department of Astronomy, Oskar Klein Centre, Stockholm University, AlbaNova University Centre, SE-106 91 Stockholm, Sweden
[15] Jodrell Bank Centre for Astrophysics, University of Manchester, Oxford Road, Manchester UK
[16] Department of Astronomy, University of Maryland, College Park, MD 20742, USA
[17] Observational Cosmology Lab, NASA Goddard Space Flight Center, Greenbelt, MD 20771, USA
[18] Center for Research and Exploration in Space Science and Technology, NASA/GSFC, Greenbelt, MD 20771, USA
[19] INAF—OAS, Osservatorio di Astrofisica e Scienza dello Spazio di Bologna, via Gobetti 93/3, I-40129 Bologna, Italy
Received 2023 January 5; revised 2023 February 6; accepted 2023 February 6; published 2023 March 14

Abstract

We study the spatially resolved stellar populations of 444 galaxies at $0.3 < z < 6.0$ in two clusters (WHL 0137–08 and MACS 0647+70) and a blank field, combining imaging data from the Hubble Space Telescope and JWST to perform spatially resolved spectral energy distribution (SED) modeling using PIXEDFIT. The high spatial resolution of the imaging data combined with magnification from gravitational lensing in the cluster fields allows us to resolve a large fraction of our galaxies (109) to subkiloparsec scales. At redshifts around cosmic noon and higher ($2.5 \lesssim z \lesssim 6.0$), we find mass-doubling times to be independent of radius, inferred from flat specific star formation rate (sSFR) radial profiles and similarities between the half-mass and half-SFR radii. At lower redshifts ($1.5 \lesssim z \lesssim 2.5$), a significant fraction of our star-forming galaxies shows evidence for nuclear starbursts, inferred from a centrally elevated sSFR and a much smaller half-SFR radius compared to the half-mass radius. At later epochs, we find more galaxies suppress star formation in their centers but are still actively forming stars in the disk. Overall, these trends point toward a picture of inside-out galaxy growth consistent with theoretical models and simulations. We also observe a tight relationship between the central mass surface density and global stellar mass with ∼0.38 dex scatter. Our analysis demonstrates the potential of spatially resolved SED analysis with JWST data. Future analysis with larger samples will be able to further explore the assembly of galaxy mass and the growth of their structures.

Unified Astronomy Thesaurus concepts: Galaxy evolution (594); Galaxy formation (595); Galaxy clusters (584); Galaxy quenching (2040)

1. Introduction

Over the last few decades, multiwavelength studies of galaxies throughout cosmic history reveal that the global star formation rate density (SFRD) in the universe was increasing with cosmic time from the reionization epoch and reached a peak at $z \sim 2$ (∼3.5 Gyr after the Big Bang; cosmic noon), after which it declined exponentially toward the present day (Madau & Dickinson 2014). In this picture, it is estimated that ∼25% of the present-day stellar-mass density (SMD) was formed before the peak of the cosmic SFRD, around half of the SMD was formed during $0.7 < z < 2.0$, and another ∼25% had formed since $z = 0.7$ (i.e., around the last half of the universe's age; Madau & Dickinson 2014). Although the cosmic SFRD at early cosmic time is still debated due to the dust obscuration effects (see e.g., Casey et al. 2018; Fudamoto et al. 2021), an emerging picture is that cosmic SMD increases with cosmic time from the epoch of reionization, which is believed to take

[20] Hubble Fellow.

place before $z \sim 6$ (e.g., Treu et al. 2013; McGreer et al. 2015; Dayal & Ferrara 2018).

Observations also revealed that most of the star formation occurs in galaxies that lie in the so-called star-forming main sequence (SFMS), which is a tight nearly linear correlation between the integrated (i.e., global) star formation rate (SFR) and stellar mass (M_*; Brinchmann et al. 2004; Daddi et al. 2007; Elbaz et al. 2007; Noeske et al. 2007; Whitaker et al. 2012; Speagle et al. 2014; Whitaker et al. 2014; Salmon et al. 2015; Tomczak et al. 2016; Santini et al. 2017; Iyer et al. 2018; Leslie et al. 2020; Leja et al. 2022; Popesso et al. 2023). This relation has been shown to hold at any epoch with a nearly constant scatter (∼0.3 dex; Whitaker et al. 2012; Speagle et al. 2014; Popesso et al. 2023), suggesting that galaxies grow in mass over cosmic time in a state of self-regulated semiequilibrium (e.g., Bouché et al. 2010; Daddi et al. 2010; Genzel et al. 2010; Tacchella et al. 2016b, 2020). Understanding this process in detail and the mechanisms that shut down star formation in galaxies and move them out of the SFMS onto the "quenched" population requires knowledge of not only integrated galaxy properties but also spatially resolved structures within galaxies.

The study of spatially resolved properties of galaxies with integral field spectroscopy (IFS) and high-spatial-resolution imaging has been providing important insights toward a better understanding of galaxy evolution. Among the important findings is the realization that some of the well-known scaling relations observed on global scales originated from similar relations on kiloparsec scales within galaxies (see a review by Sánchez 2020). This includes the spatially resolved SFMS (rSFMS), a relationship between the SFR surface density ($\Sigma_{\rm SFR}$) and M_* surface density (Σ_*), a local analog of the global SFMS (e.g., Sánchez et al. 2013; Wuyts et al. 2013; Cano-Díaz et al. 2016; Abdurro'uf & Akiyama 2017; Hsieh et al. 2017; Abdurro'uf & Akiyama 2018; Lin et al. 2019; Enia et al. 2020). Recent studies found that the rSFMS relation (and hence the global SFMS) originated from two more fundamental relations on kiloparsec scales: the resolved Kennicutt–Schmidt ($\Sigma_{\rm SFR}$ versus H_2 mass surface density; Σ_{H_2}) and molecular gas main-sequence relations (Σ_* versus Σ_{H_2}) (e.g., Lin et al. 2019; Morselli et al. 2020; Abdurro'uf et al. 2022b; Baker et al. 2022). This emphasizes the necessity of studying the spatially resolved properties of galaxies.

Spatially resolved studies of high-redshift galaxies ($z \sim 1$–4) have hinted at how galaxies assembled their structures. The emerging picture from these studies is that galaxies grow their mass in an inside-to-outside manner (i.e., inside-out growth scenario; e.g., Nelson et al. 2012; van Dokkum et al. 2013; Morishita et al. 2015; Nelson et al. 2016) and cease their star formation activities in a similar manner (i.e., the inside-out quenching scenario; e.g., Tacchella et al. 2015; Jung et al. 2017; Abdurro'uf & Akiyama 2018; Ellison et al. 2018; Tacchella et al. 2018; Bluck et al. 2020). Nelson et al. (2016) analyzed the spatially resolved distributions (on kiloparsec scales) of Hα emission and stellar mass of $0.7 < z < 1.5$ galaxies using the Hubble Space Telescope (HST)/WFC3 grism data from the 3D-HST survey (Skelton et al. 2014). They found that the spatial distribution of H_α emission in the galaxies is more extended than the stellar-mass distribution, suggesting that past star formation in galaxies has accumulated stellar mass in the center and now the star formation progresses outward to assemble the disk. Tacchella et al. (2015) analyzed the spatial distributions of SFR and M_* of ∼30 star-forming galaxies at $z \sim 2$ using IFS data from the SINS/zC-SINF survey (Förster Schreiber et al. 2018). They observed that massive galaxies ($M_* \gtrsim 10^{11} M_\odot$) in their sample have a centrally suppressed specific SFR (sSFR) radial profile and a massive central spheroid that is as dense as the centers of local early-type galaxies. In contrast to this, less-massive galaxies in their sample have broadly flat sSFR radial profiles. This trend indicates that massive galaxies at this epoch might have started a quenching process in their central regions and assembled a mature bulge.

The buildup of the central stellar-mass density is likely correlated with the quenching process in galaxies. The central stellar-mass density within a 1 kpc radius ($\Sigma_{*,1\rm kpc}$) has been shown to be a good predictor for quiescence, where galaxies with high $\Sigma_{*,1\rm kpc}$ tend to be red and quiescent, whereas galaxies with low $\Sigma_{*,1\rm kpc}$ tend to be blue and star-forming (e.g., Fang et al. 2013; Tacchella et al. 2015, 2016a; Barro et al. 2017; Jung et al. 2017; Whitaker et al. 2017; Dimauro et al. 2022). It has also been shown that $\Sigma_{*,1\rm kpc}$ is tightly correlated with the global M_*, suggesting that M_* of galaxies grow hand in hand with the central mass density. In this $\Sigma_{*,1\rm kpc}$–M_* relation, quiescent galaxies reside in a sequence at the tip of the overall relationship and have a shallower slope than the relation with star-forming galaxies only, indicating a formation of a matured bulge in the quiescent galaxies (Fang et al. 2013; Tacchella et al. 2015; Barro et al. 2017).

Galaxies also grow their sizes hand in hand with the global M_*, as indicated by the size–mass relation (e.g., Shen et al. 2003; van der Wel et al. 2014; Suess et al. 2019). Previous studies have shown that star-forming and quiescent galaxies follow very different size–mass relations where quiescent galaxies tend to be more compact (i.e., having smaller size) in all M_* and exhibit a steeper relation than star-forming galaxies (van der Wel et al. 2014; Yang et al. 2021). A possible explanation for this trend is that star-forming galaxies build their mass at all radii by mostly in situ star formation, whereas quiescent galaxies grow inside-out through mergers (e.g., van Dokkum et al. 2015).

Previous studies, some of which are mentioned above, have used HST for resolving galaxies out to $z \sim 3$, roughly a limit where galaxies can be resolved well by the telescope, given its spatial resolution and depth. Furthermore, the wavelength coverage of HST only covers the rest-frame ultraviolet (UV) and a small portion of the optical at $z \sim 3$, making it difficult to robustly derive M_* as well as the other stellar population properties, which typically requires a rest-frame near-infrared (NIR). Forcing the inclusion of NIR imaging from ground-based telescopes would need the spatial resolution of HST to be sacrificed (e.g., Jung et al. 2017). With the advent of the James Webb Space Telescope (JWST) NIRCam observations (Rieke et al. 2022; Rigby et al. 2022), with its high spatial resolution, depth, and its coverage in NIR, now we can push the analysis of the spatially resolved spectral energy distribution (SED) of galaxies to higher redshifts. Some very recent studies have used JWST/NIRCam imaging to study the internal structures and morphology of galaxies at $z > 3$ (e.g., Chen et al. 2022; Ferreira et al. 2022; Giménez-Arteaga et al. 2022; Kartaltepe et al. 2022; Pérez-González et al. 2022), even resolving a lensed galaxy at $z \sim 11$ (Hsiao et al. 2022).

In this paper, we use imaging data from HST/ACS and JWST/NIRCam to analyze the spatially resolved SEDs of $0.3 < z < 6.0$ galaxies in the sight lines of the

WHL J013719.8–082841 (hereafter WHL 0137−08; R.A. = 01:37:25.0, decl. = −08:27:23, J2000; $z = 0.566$; Wen et al. 2012; Wen & Han 2015) and MACS J0647.7+7015 (hereafter MACS 0647+70; R.A. = 06:47:50.03, decl. = +70:14:49.7, J2000; $z = 0.591$; Ebeling et al. 2007) clusters and examine the spatial distributions of their stellar populations. Our main goal is to get hints on the assembly of galaxy structures over cosmic time, especially how galaxies build their stellar masses and quench their star formation activities. The high spatial resolution of JWST/NIRCam, combined with magnification from gravitational lensing in the cluster fields, allows us to resolve high-redshift galaxies down to subkiloparsec scales. Our method using PIXEDFIT (Abdurro'uf et al. 2022c) can simultaneously process imaging data, perform pixel binning to optimize the signal-to-noise ratio (S/N) of the spatially resolved SEDs, and perform SED fitting. The wavelength coverage of HST/ACS and JWST/NIRCam allows us to get full coverage of the rest-frame UV to NIR for the majority of our sample, which can give a strong constraint on model SEDs and break the age–dust–metallicity degeneracy (see Appendix B). While IFS observation at $z \gtrsim 2$ is lacking, our analysis in this paper provides a good alternative for the analysis of spatially resolved SEDs of high-redshift galaxies. Our analysis in this paper is one of the first robust spatially resolved SED analyses of hundreds of galaxies using JWST data. Abdurro'uf et al. (2021) have demonstrated the capabilities of spatially resolved SED fitting using PIXEDFIT on local galaxies. In particular, it gives a robust SFR on kiloparsec scales when rest-frame UV–NIR photometry is available, which is consistent with the SFR derived from Hα emission maps (dust-corrected based on the Balmer decrement) from the MaNGA IFS survey (Bundy et al. 2015).

The paper is organized as follows. In Section 2, we present the data and sample galaxies. We describe the spatially resolved SED-fitting methodology in Section 3 and present our results in Section 4, which include the radial profiles of some key stellar population properties, a comparison between the compactness of the spatial distributions of SFR and M_*, and the $\Sigma_{*,1\mathrm{kpc}}$–M_* relation. In Section 5, we further discuss our results, focusing on the evolutionary trends with redshift and the implications to the study of galaxy evolution.

Throughout this paper, we assume the Chabrier (2003) initial mass function (IMF) with a mass range of 0.1–100$M_\odot$ and cosmological parameters of $\Omega_m = 0.3$, $\Omega_\Lambda = 0.7$, and $H_0 = 70\ \mathrm{km\ s^{-1}\ Mpc^{-1}}$.

2. Data and Sample

2.1. Observational Data

2.1.1. JWST Observations

We obtain JWST/NIRCam imaging data of the WHL 0137−08 cluster from Cycle 1 General Observers (GO) 2282 program (PI Coe) and the MACS 0647+70 cluster from the GO 1433 program (PI Coe). The WHL 0137−08 cluster was observed in 2022 July, while the MACS 0647+70 cluster was observed on 2022 September 23. The GO 2282 program aims to further investigate Earendel (Welch et al. 2022a, 2022b) and the Sunrise Arc (Vanzella et al. 2022). The JWST/NIRCam data from this program consist of eight filters (F090W, F115W, F150W, F200W, F277W, F365W, F410M, and F444W), spanning a wavelength range of 0.8–5.0 μm. The GO 1433 program is intended to observe the triply lensed galaxy MACS 0647JD at $z \sim 11$ (Coe et al. 2013; Hsiao et al. 2022). This program obtained JWST/NIRCam imaging in six filters (F115W, F150W, F200W, F277W, F365W, and F444W) spanning 1–5 μm. The exposure time of each filter in the two programs is 2104 s. It achieves a 5σ limiting AB magnitude of 28.0–29.0 in an $r = 0\farcs2$ diameter circular aperture.

For each filter, we obtained four dithers using INTRAMODULEBOX primary dithers to cover the 4″–5″ gap between the short-wavelength (SW; $\lambda < 2.4\ \mu$m) detectors, improve the spatial resolution of final drizzled images, and minimize the impact of image artifacts and bad pixels. In each observation, we obtained NIRCam imaging over two $2\farcm26 \times 2\farcm26$ fields separated by $40\farcs5$, covering a total area of 10.2 arcmin^2. In the observation of the WHL 0137−08 cluster, the NIRCam module B was centered at the cluster while module A covered a nearby field centered $\sim 2\farcm9$ from the cluster center (hereafter called "blank field"). On the other hand, the MACS 0647+70 cluster was centered at module A, and module B observed a blank field nearby to it.

2.1.2. HST Data

We obtain HST imaging data of the WHL 0137−08 cluster from the Reionization Lensing Cluster Survey (RELICS) HST Treasury program (GO 14096; Coe et al. 2019). The RELICS program obtained the first HST imaging of the WHL 0137−08 cluster in 2016 with three orbits of ACS (F435W, F606W, and F814W) and two orbits of WFC3/IR (F105W, F125W, F140W, and F160W) data spanning 0.4–1.7 μm. Two follow-up HST imaging programs (GO 15842 and GO 16668; PI: Coe) have thus far obtained an additional five orbits of HST ACS imaging in F814W, two orbits in F475W, and four orbits with WFC3/IR in F110W.

The HST imaging data of the MACS 0647+70 cluster are taken from multiple programs. Overall, MACS 0647+70 has been observed in a total of 39 orbits of HST imaging in 17 filters. The cluster was first observed by programs GO 9722 (PI Ebeling) and GO 10493 and 10793 (PI Gal-Yam) in the ACS F555W and F814W filters. Then additional imaging in 15 filters (WFC3/UVIS, ACS, and WFC3/IR, spanning 0.2–1.7 μm) was obtained by the Cluster Lensing and Supernova Survey with Hubble (CLASH; Postman et al. 2012; GO 12101, PI Postman). Finally, additional imaging in WFC3/IR F140W was obtained as part of a grism spectroscopy program (GO 13317, PI Coe).

It is important to note that the blank fields near the WHL 0137−08 and MACS 0647+70 clusters that were observed with NIRCam are not covered in the HST observations described above. In this work, we analyze galaxies in three fields: the WHL 0137−08 cluster field, the MACS 0647+70 cluster, and the NIRCam blank field near WHL 0137−08 (hereafter simply called blank field). We do not analyze galaxies in the NIRCam blank field of MACS 0647+70 because it is observed in fewer filters than the blank field of WHL 0137−08 and it does not have F090W observation, which prevents us from selecting galaxies at $z < 2$ in this field as their photometry do not cover the rest-frame 4000 Å break. For WHL 0137−08 and the blank field, we use four HST/ACS filters (F435W, F475W, F606W, and F814W) and eight JWST/NIRCam filters, whereas for MACS 0647+70, we use seven HST/ACS filters (F435W, F475W, F555W, F606W, F625W, F775W, and F814W) and six JWST/NIRCam filters. We do not use HST/WFC3 IR filters to get as high a spatial

Table 1
HST and JWST Imaging Data Used in the Spatially Resolved SED Fitting

Telescope	Camera	Filter	Wavelength (μm)	Depth[a]		PSF FWHM[b]	
				WHL 0137−08 (AB mag)	MACS 0647+70 (AB mag)	WHL 0137−08 (arcsec)	MACS 0647+70 (arcsec)
HST	ACS/WFC	F435W	0.37–0.47	27.7	28.0	0.11	0.11
HST	ACS/WFC	F475W	0.4–0.55	28.5	28.2	0.11	0.11
HST	ACS/WFC	F555W	0.46–0.62	⋯	28.7	⋯	0.11
HST	ACS/WFC	F606W	0.47–0.7	28.3	28.3	0.11	0.11
HST	ACS/WFC	F625W	0.54–0.71	⋯	27.9	⋯	0.11
HST	ACS/WFC	F775W	0.68–0.86	⋯	27.8	⋯	0.08
HST	ACS/WFC	F814W	0.7–0.95	28.7	28.5	0.11	0.11
JWST	NIRCam	F090W	0.8–1.0	28.3	⋯	0.04	⋯
JWST	NIRCam	F115W	1.0–1.3	28.4	28.1	0.04	0.04
JWST	NIRCam	F150W	1.3–1.7	28.5	28.3	0.06	0.06
JWST	NIRCam	F200W	1.7–2.2	28.7	28.4	0.06	0.06
JWST	NIRCam	F277W	2.4–3.1	29.1	28.9	0.11	0.11
JWST	NIRCam	F356W	3.1–4.0	29.3	29.0	0.11	0.11
JWST	NIRCam	F410M	3.8–4.3	28.6	⋯	0.16	⋯
JWST	NIRCam	F444W	3.8–5.0	29.0	28.8	0.16	0.16

Notes.
[a] 5σ point-source AB magnitude limit measured within a $0\farcs2$ diameter circular aperture.
[b] PSF FWHM is based on empirical measurement as described in Appendix C.

resolution as possible while still getting sufficiently wide wavelength coverage with the HST/ACS and JWST/NIRCam. Please refer to Table 1 for information on limiting magnitudes and the point-spread function (PSF) sizes of our data.

2.2. Sample Galaxies

We use the GRIZLI v4 photometric catalogs (which will be described in Section 3.1) to select our sample galaxies in the three fields (WHL 0137−08, blank field, and MACS 0647+70). The catalogs provide aperture fluxes and photometric redshifts with which we select our sample. The sample selection is described in the following. First, we select galaxies that have an integrated S/N > 5 in all JWST filters that are available for the fields. This is to ensure that we will have galaxies with good photometry in at least the JWST filters. This initial cut selects 1322 (out of 2718), 1278 (out of 3032), and 1331 (out of 2660) galaxies in WHL 0137−08, blank field, and MACS 0647+70, respectively. We do not apply the same S/N criteria on HST filters because it would exclude more galaxies as they have lower S/N than JWST filters.

We further cut the sample galaxies based on their redshift to get sufficient coverage of the rest-frame UV–NIR. For galaxies in WHL 0137−08 and MACS 0647+70, which are observed by both JWST and HST, we select galaxies at $0.3 < z < 6.0$, whereas for galaxies in the blank field, which do not have HST observations, we select galaxies at $1.3 < z < 6.0$. This redshift cut ensures that the rest-frame 4000 Å break is covered. This cut further reduces the sample to 1258, 581, and 1257 galaxies in WHL 0137−08, the blank field, and MACS 0647+70, respectively. After that, we do a visual inspection to exclude galaxies that appear to be very small (i.e., unresolved) and in a merger (i.e., one segmentation region having multiple cores or multiple galaxies in one segmentation region, despite possible interlopers). This further reduces the sample to 354, 239, and 220 galaxies in WHL 0137−08, the blank field, and MACS 0647+70, respectively.

We perform spatially resolved SED analysis on the galaxies in this initial sample. A detailed description of the methodology will be given in Section 3. Once the analysis is done, we inspect the results of all the galaxies and further exclude galaxies that seem to have bad SED-fitting results based on the χ^2 values of the fitting to the integrated SEDs within the central effective radius (see Section 3.5) and the average χ^2 values of the fitting to the first 20 spatial bins (see Section 3.4 for the definition of the spatial bin). We exclude galaxies that have $\chi^2 > 20$ for the SEDs within the central effective radius and average $\chi^2 > 40$ for the first 20 spatial bins. We note that the χ^2 value can be unrealistically high if systematic uncertainties of the photometry are not properly accounted for. Besides this, there is still uncertainty around the zero-point calibration of NIRCam photometry in the current early observations (e.g., Boyer et al. 2022; Finkelstein et al. 2022). Therefore, we visually inspect the SED-fitting results of each galaxy using similar plots to those shown in Figure 4. We find that in most cases, NIRCam fluxes are well fitted by our models, better than HST/ACS fluxes. This might be due to the shallower depths (and lower S/N) of HST compared to JWST. The χ^2 values above are high enough to get a sufficient number of galaxies and low enough to get good-quality SED-fitting results. This results in our final sample, consisting of 243, 91, and 110 galaxies in WHL 0137−08, the blank field, and MACS 0647+70, respectively. Figure 1 shows the distributions of redshifts and M_* of our sample galaxies.

We note that our sample selection may be possibly biased toward selecting relatively massive, bright, and resolved (i.e., big) galaxies in each redshift. However, due to the lensing magnification in the cluster fields, we expect to detect on average lower-mass galaxies with better spatial resolution than in the normal fields. The small number of galaxies and the limited volume sampled might make our sample to be not representative of the general population of galaxies. However, since we do not make inferences on the average trends or number densities as a function of global properties (e.g., M_*), but instead we show trends in individual galaxies, our results

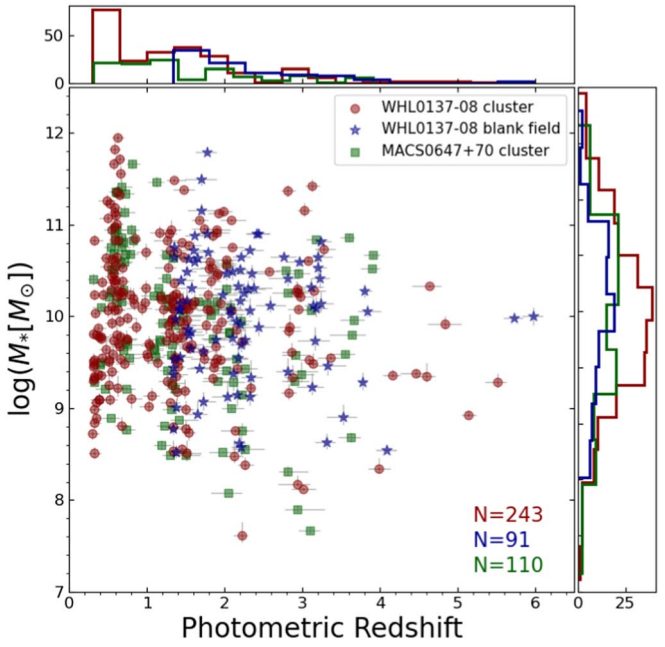

Figure 1. Distributions of M_* and redshifts of the sample galaxies analyzed in this work, which consists of galaxies in two cluster fields (WHL 0137−08 and MACS 0647+70) and a blank field (a nearby field centered ∼2.′9 from WHL 0137−08 that was observed with JWST/NIRCam). The global M_* shown here are derived by summing up the M_* of pixels (in the galaxy's region) obtained from our spatially resolved SED fitting.

still provide useful insights into the evolution of galaxy structures. We also ignore the possible contamination by active galactic nucleus (AGN) host galaxies in our current study because of the lack of diagnostics for identifying them using our current data.

3. Methodology

3.1. Data Reduction and Photometric Catalog

We use the GRIZLI pipeline (Brammer et al. 2022) to process the HST FLT and the JWST pipeline-calibrated level-2 imaging data. The JWST data were processed using the calibration pipeline v1.5.3 with CRDS context `jwst_0942.pmap`, which includes photometric calibrations based on in-flight data. The JWST level-2 imaging data were then scaled with detector-dependent factors (Brammer 2022) based on a NIRCam flux calibration using the standard star J1743045. Our photometric zero-points described here are similar to those obtained by the JWST Resolved Stellar Populations ERS program (Boyer et al. 2022; Nardiello et al. 2022), which analyzed the M92 globular cluster. We also check the consistency of our calibration with the more recent one based on CAL program data `jwst_0989.pmap` and find out that they are consistent within 3% in all filters analyzed here.

In processing the JWST data, the GRIZLI pipeline applies a correction to reduce the effect of $1/f$ noise and masks the "snowballs"[22] effect caused by the large cosmic-ray impacts on the NIRCam detectors. Besides this, the GRIZLI pipeline also corrects for "wisps,"[23] which are faint, diffuse stray-light features that appear at the same detector locations in NIRCam images and are most prominent in the A3, B3, and B4 detectors in the F150W and F200W images.

The GRIZLI pipeline aligns the HST and JWST imaging data to a common world coordinate system that is registered based on the GAIA DR3 catalogs (Gaia Collaboration et al. 2021). The images are then drizzled to a common pixel grid using ASTRODRIZZLE (Koekemoer et al. 2003; Hoffmann et al. 2021). The 17 HST filters and 4 JWST NIRCam long-wavelength (LW) filters (F277W, F356W, F410M, and F444W) are drizzled to a spatial sampling of 0.″04 per pixel while the JWST SW filters (F090W, F115W, F150W, and F200W) are drizzled to a spatial sampling of 0.″02 per pixel.

Source detection is then performed on a weighted sum of the drizzled NIRCam images in all filters using SEP (Bertin & Arnouts 1996; Barbary 2016). Fluxes are then calculated for each source in three circular apertures, 0.″36, 0.″5, and 0.″7. Then photometric redshift measurement is performed using the 0.″5 aperture SEDs employing EAZYPY (Brammer et al. 2008). This code fits observed photometry using a set of templates added in a nonnegative linear combination. The processed imaging data along with the photometric catalog are publicly available.[24] These data products have also been used in some recent studies (Bradley et al. 2022b; Welch et al. 2022b; Hsiao et al. 2022; Meena et al. 2023; Vanzella et al. 2022).

3.2. Analysis of Postprocessed Imaging Data

In this work, we combine the postprocessed HST and JWST imaging data (in up to 13 filters) into a common spatial resolution (i.e., PSF size) and sampling (i.e., pixel size) for extracting the spatially resolved SEDs of our sample galaxies. These spatially resolved SEDs are then fitted with models to infer the underlying properties of the stellar populations. We use PIXEDFIT[25] (Abdurro'uf et al. 2021, 2022c) throughout this analysis. Basically, this process includes three main tasks: image processing, pixel binning, and SED fitting. We will briefly describe these steps in the following.

The image processing is carried out automatically using PIXEDFIT. For each galaxy, we first crop stamp images with a size of 6.″04×6.″04 (corresponding to 302 ×302 pixels in NIRCam SW and 151 ×151 pixels in the NIRCam LW and HST/ACS filters) centered at the galaxy. We then perform background subtraction to each stamp image using PHOTUTILS (Bradley et al. 2022a). Next, we perform PSF matching to homogenize the spatial resolution across filters. We degrade the spatial resolution of the images to match the resolution of the F444W filter, which has the lowest spatial resolution (see Table 1). For this, we generate the empirical PSFs of the HST/ACS and JWST/NIRcam filters along with the convolution kernels using the PHOTUTILS package (see Appendix C). The PSF matching is carried out by convolving the stamp images with the convolution kernels. After PSF matching, we register all the stamp images to a common spatial sampling of 0.″04 per pixel. In the end, we have multiband stamp images with a size of 151 × 151 pixels for each galaxy in our sample.

[21] https://jwst-docs.stsci.edu/data-artifacts-and-features/snowballs-and-shower-artifacts
[22] https://jwst-docs.stsci.edu/jwst-near-infrared-camera/nircam-features-and-caveats/nircam-claws-and-wisps
[23] https://cosmic-spring.github.io/index.html
[24] https://github.com/aabdurrouf/piXedfit

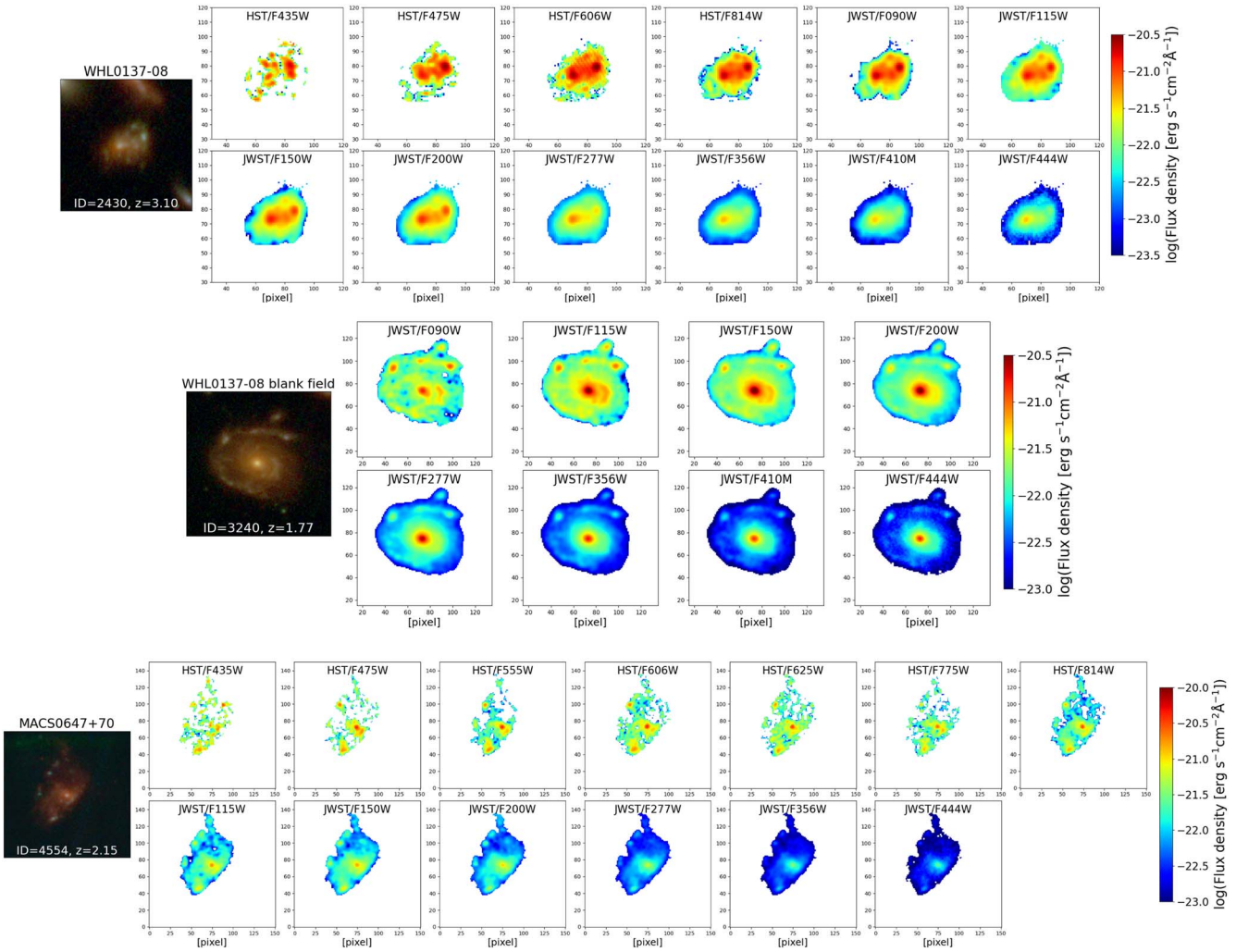

Figure 2. Examples of the maps of multiband fluxes produced from image processing. An example of one galaxy is shown for each field, from top to bottom: WHL 0137−08 (observed in 12 filters), blank field (8 filters), and MACS 0647+70 (13 filters). The galaxy ID is based on our GRIZLI v4 public catalog.

3.3. Constructing Photometric Data Cubes

PIXEDFIT further processes the stamp images to produce photometric data cubes. First, it defines a galaxy's region of interest. For each galaxy, segmentation maps are first produced in all filters using SEP (Barbary 2016), and those maps are then merged together into a single map. In the segmentation process, we use the same parameters for all filters as follows. We set the detection threshold (`thresh`), the number of thresholds for deblending (`deblend_nthresh`), and the minimum contrast ratio for deblending (`deblend_cont`) to be 2.0, 40, and 0.005, respectively.

In some cases, the merged segmentation map is larger than expected, as can be inferred from the maps of multiband fluxes. This can be caused by some factors, for example, interference from neighboring objects that are not separated well by the deblending process. We visually inspect the merged segmentation map of each galaxy to find out this issue. To deal with this, we tweak the deblending parameters to get cleaner segmentation maps or ignore the segmentation map in some filters that have this deblending issue, then merge them again.

Once the galaxy's region is defined, then the fluxes of pixels within the region are calculated. We use the PHOTFLAM keyword in the header of the GRIZLI imaging data products to convert the pixel value into flux density in units of erg s^{-1} cm^{-2} $Å^{-1}$. The data cubes are then stored in FITS files. Figure 2 shows examples of the maps of multiband fluxes of galaxies in the three fields analyzed in this work. The color images shown in the leftmost panels are created using `Trilogy`[26] (Coe et al. 2012).

3.4. Pixel Binning

The SEDs of pixels are usually noisy and might not provide sufficient constraint to the models if the fitting is performed on them. Therefore, we perform pixel binning using PIXEDFIT to optimize the S/N of the spatially resolved SEDs. Basically, this process bins neighboring pixels to achieve a certain S/N threshold that can be set in multiple bands. The unique pixel-binning scheme in PIXEDFIT, which takes into account the similarity in SED shape among pixels, allows for a sufficient S/N to be achieved in multiple filters of interest while preserving important spatial information at the pixel level. A detailed description of this pixel-binning scheme is given in Abdurro'uf et al. (2021).

We assume the following parameters in the pixel-binning process. We refer the reader to Abdurro'uf et al. (2021) for more information about the parameters. We set S/N thresholds

[25] https://github.com/dancoe/trilogy

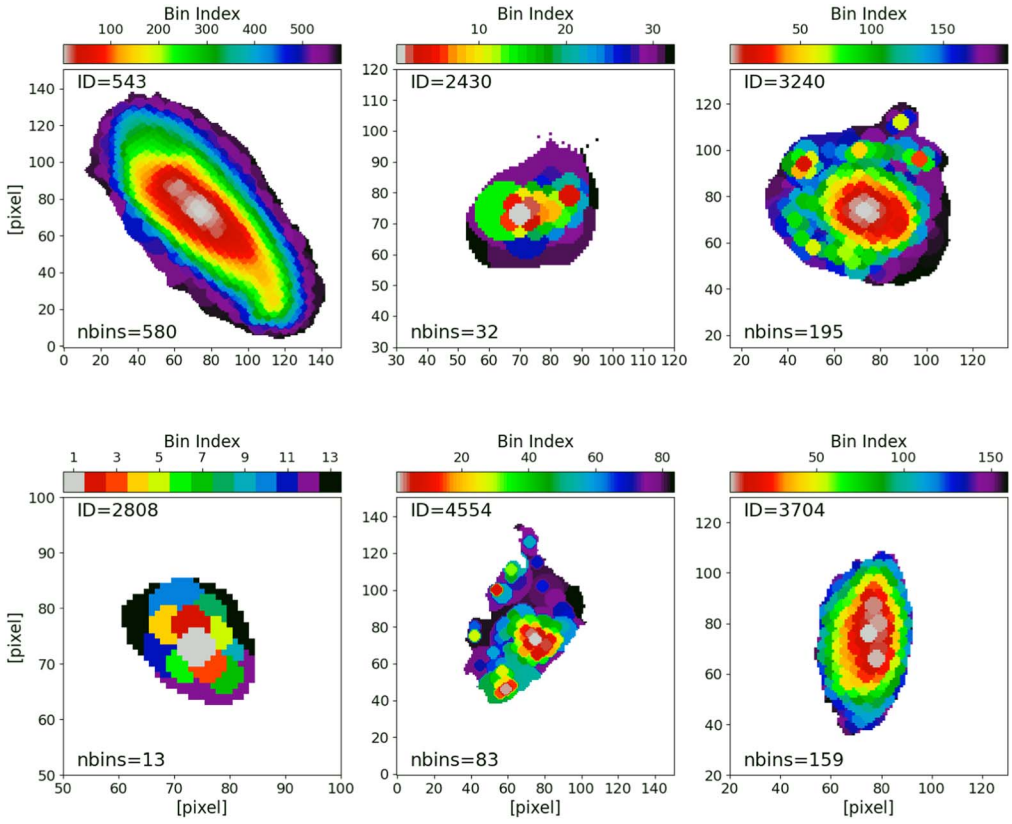

Figure 3. Examples of pixel-binning results. The pixel-binning process achieves a minimum S/N of 5 in all JWST NIRCam filters.

to 5 in all JWST NIRCam filters. We do not set the S/N threshold to HST filters because the S/N of pixels in the HST images is low, especially for galaxies at high redshifts. Setting an S/N threshold on the HST filters would put a strong constraint on the pixel-binning process, which can produce a coarser binning map and lose important spatial information from the original images.

The rest of the binning parameters are as follows. We set a minimum diameter of 7 pixels, which is larger than the PSF FWHM size of our data cubes, a reduced χ^2 limit of 5 in the evaluation of the similarity of SED shape. We refer to the F277W flux in determining the brightest pixel to be the center of a spatial bin. We store new data cubes produced from this pixel-binning process into FITS files. The total number of spatial bins in our sample galaxies is 24,999. Figure 3 shows examples of the pixel-binning maps produced from this process.

3.5. Spatially Resolved SED Fitting

Once we have the binned data cubes, we perform SED fitting to the SEDs of individual spatial bins in our sample galaxies. Here we use the SED-fitting module in PIXEDFIT. The SED fitting in PIXEDFIT uses a fully Bayesian technique. We refer the reader to Abdurro'uf et al. (2021) for a detailed description of the SED-modeling and -fitting methods as well as comprehensive tests of its capabilities. In Appendix A, we perform SED-fitting tests using mock SEDs to demonstrate the robustness of our SED-fitting method on combined HST and JWST photometry. Moreover, in Appendix B we discuss how NIRCam photometry can potentially help break the degeneracies among age, dust, and metallicity in SED fitting. In the following, we provide a brief description of the method and some assumptions applied in our SED fitting.

We use the Flexible Stellar Population Synthesis code (FSPS; Conroy et al. 2009; Conroy & Gunn 2010). It includes the nebular emission modeling that uses the CLOUDY code (Ferland et al. 1998, 2013). In this work, we assume the Chabrier (2003) IMF, Padova isochrones (Girardi et al. 2000; Marigo & Girardi 2007; Marigo et al. 2008), and MILES stellar spectral library (Sánchez-Blázquez et al. 2006; Falcón-Barroso et al. 2011). For the star formation history model, we assume an analytic model in the form of a double power law. It has been shown in Abdurro'uf et al. (2021) that this SFH form can give robust inferences of the stellar population properties and even SFH of galaxies, as tested using synthetic SEDs of simulated galaxies in the IllustrisTNG simulations. To simulate the effect of dust attenuation, we use the two-component dust attenuation law of Charlot & Fall (2000). This dust attenuation law gives an extra attenuation to stars younger than 10 Myr, in addition to standard attenuation in the diffuse ISM. We model the attenuation due to the intergalactic medium using the Inoue et al. (2014) model. Since we do not have photometric data that cover the rest-frame mid-infrared (MIR) and far-infrared (FIR), we switch off the modeling of dust emission and AGN dusty torus emission in the analysis throughout this work. The SED modeling has nine free parameters. We summarize these parameters along with the assumed priors in Table 2. We assume a constant ionization parameter (U) of 0.01 in the modeling of the nebular emission.

In the current analysis, we rely on photometric redshift for all of our sample galaxies because we do not have spectroscopic observations at the moment we carry out this analysis. To get redshift estimates of the galaxies, we perform SED fitting with

Table 2
Free Parameters in the SED Modeling and the Assumed Priors

Parameter	Description	Prior	Sampling/Scale
M_*	Stellar mass	Uniform: min $=\log(s_{\rm best}) - 2$, max $=\log(s_{\rm best}) + 2$[a]	Logarithmic
Z_*	Stellar metallicity	Uniform: min $=-2.0 + \log(Z_\odot)$, max $=0.2 + \log(Z_\odot)$	Logarithmic
t	Time since the onset of star formation (age_{sys})[b]	Uniform: min $=-1.0$, max = age of the universe at the galaxy's redshift	Logarithmic
τ	Parameter that controls the peak time in the double-power-law SFH model[b]	Uniform: min $=-1.5$, max $=1.14$	Logarithmic
α	Parameter in the double-power-law SFH model that controls the slope of the falling star formation episode[b]	Uniform: min $=-2.0$, max $=2.0$	Logarithmic
β	Parameter in the double-power-law SFH model that controls the slope of the rising star formation episode[b]	Uniform: min $=-2.0$, max $=2.0$	Logarithmic
$\hat{\tau}_1$	Dust optical depth of the birth cloud in the Charlot & Fall (2000) dust attenuation law	Uniform: min $=0.0$, max $=4.0$	Linear
$\hat{\tau}_2$	Dust optical depth of the diffuse ISM in the Charlot & Fall (2000) dust attenuation law	Uniform: min $=0.0$, max $=4.0$	Linear
n	Power-law index in the Charlot & Fall (2000) dust attenuation law	Uniform: min $=-2.2$, max $=0.4$	Linear

Notes.
[a] $s_{\rm best}$ is the normalization of the model SED derived from the initial fitting with the χ^2-minimization method (see Section 4.2.1 in Abdurro'uf et al. 2021).
[b] The mathematical form of the double-power-law SFH is given in Abdurro'uf et al. (2021, Equation (7) therein).

PIXEDFIT in which the redshift is left free in the fitting. For this, we fit the integrated SED within the effective radius of the galaxies. The effective radius is measured in the F444W image stamp using GALFIT (Peng et al. 2002; see Section 4.2). This is performed to get SEDs with high S/N while reducing contamination from noisy SEDs of pixels in the outskirt regions. In this fitting, we apply a prior on the redshift in the form of a Gaussian function centered at the photometric redshift estimated by EAZYPY taken from the GRIZLI catalog (see Section 3.1). We set a width of 0.5 for this Gaussian prior. This fitting is performed to derive redshift only. We then use this redshift information for the SED fitting of all spatial bins in the galaxy, in which we fix the redshift. We apply the Markov Chain Monte Carlo (MCMC) method in PIXEDFIT. In the SED fitting for redshift determination, we set the number of walkers to 100 and the number of steps per walker to 1000. For the SED fitting of spatial bins, we use 100 walkers and a lower number of steps per walker (600) to reduce computational time.

We show examples of SED-fitting results of two galaxies in Figure 4, one galaxy from the WHL 0137−08 cluster field (top panel) and the other galaxy from the blank field (bottom panel). For each galaxy, we show best-fit SEDs in the top-right panel. The observed and best-fit photometric SEDs are shown with square and circle symbols, respectively. The SED in black represents the integrated SED within the effective radius, while those in other colors are for five examples of spatial bins in the galaxies. The corner plot on the bottom-left side shows the posterior probability distribution functions (PPDF) of the model parameters obtained from the fitting on the integrated SED within the effective radius. Above this corner plot, we show the PDFs of the M_* and SFR of the example spatial bins. The best-fit spectra shown in the plot are drawn from the MCMC sampler chains. Therefore, it is possible to get a slight shift in wavelength between the best-fit spectra of the central SED (where z is free in the fitting) and that of the spatial bins (where z is fixed in the fitting). This wavelength shift reflects the uncertainty of the estimated redshift. Finally, in the bottom-right panel, we show the maps of stellar population properties, including the M_* surface density (Σ_*), SFR surface density ($\Sigma_{\rm SFR}$), mass-weighted age, $A_{V,1}$ ($\equiv 1.086 \times \hat{\tau}_1$), $A_{V,2}$ ($\equiv 1.086 \times \hat{\tau}_2$), and metallicity.

3.6. Lens Modeling

To estimate the magnifications due to the gravitational lensing effect by the clusters, we use the lens models constructed by our team. For the WHL 0137−08 cluster, we use the same lens models that were used for analyzing Earendel and the Sunrise Arc in Welch et al. (2022a), which were made publicly available.[27] These lens models were generated using four independent lens modeling software packages: `Light-Traces-Mass` (`LTM`, Broadhurst et al. 2005; Zitrin et al. 2009, 2015), `Glafic` (Oguri 2010), `WSLAP` (Diego et al. 2005, 2007), and `Lenstool` (Kneib et al. 1993; Jullo et al. 2007; Jullo & Kneib 2009). Please refer to Welch et al. (2022a) for detailed information about each model. Sample galaxies located in the blank field are expected to have only weak magnifications of $\mu \lesssim 1.1$. With the multiple lens models available for this cluster, we estimate the total and tangential (i.e., linear) magnifications (μ and μ_t, respectively) of each galaxy by taking the average values. In this way, we account for the modeling uncertainties. Based on the standard deviation values, we find that the magnifications do not vary a lot among the models. The median standard deviations of μ and μ_t are 0.11 and 0.10 dex, respectively.

The lens models for the MACS 0647+70 cluster have been constructed in the past using HST imaging data. The first lens model for MACS 0647+70, before the CLASH survey, was provided by Zitrin et al. (2011) using the `LTM` method. With the addition of HST imaging data from CLASH, new lens models were established using various methods, including `Lenstool`, `LTM`, `WSLAP`, and `LensPerfect` (Coe et al. 2008). These lens models have been used in previous studies in CLASH (e.g., Coe et al. 2013; Zitrin et al. 2015; Chan et al. 2017). Now with the addition of JWST NIRCam imaging data, which add on many new strongly lensed multiple-image candidates (thanks to its high spatial resolution and depth), a

[26] https://relics.stsci.edu/lens_models/outgoing/whl0137-08/

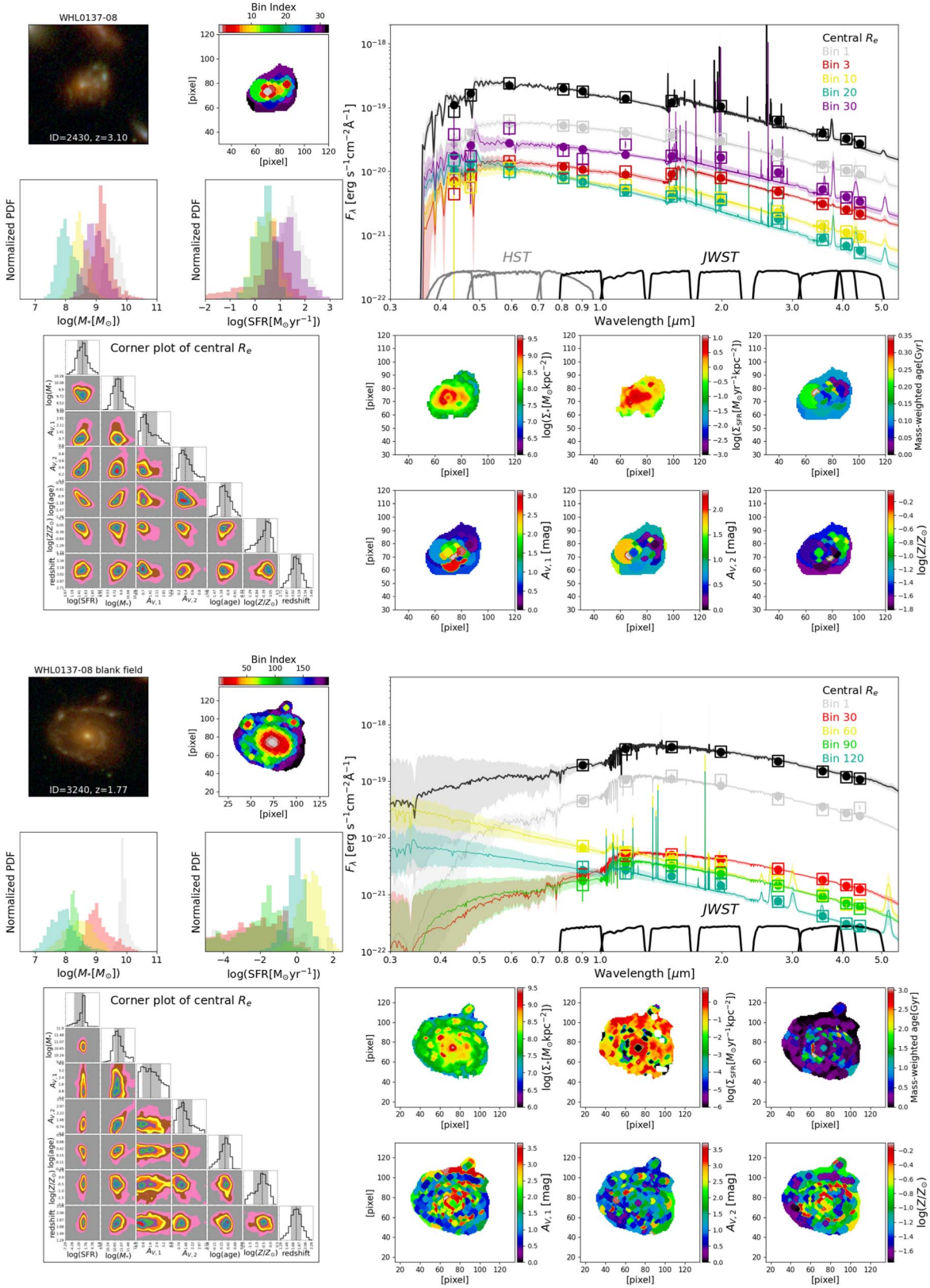

Figure 4. Examples of SED fits of a galaxy in the WHL 0137−08 cluster (top panel) and the blank field (bottom panel). The SED plots show the best-fit SEDs from the fitting to integrated SED within the effective radius (black color) and five examples of spatial bins (in colors). The corner plots show the posterior probability distributions of the parameters obtained from fitting to the central integrated SED. Above this corner plot, we show PDFs of M_* and SFR of the five example spatial bins. Finally, the maps of stellar population properties derived from this analysis are shown in the bottom-right corner.

new lens model has been established using the `dPIEeNFW` method (Zitrin et al. 2015) with some modifications. Detailed information on this lens modeling of the MACS 0647+70 cluster, along with the list of the multiple-image systems considered in the modeling, is given in Meena et al. (2023). This new method has also been implemented in several clusters

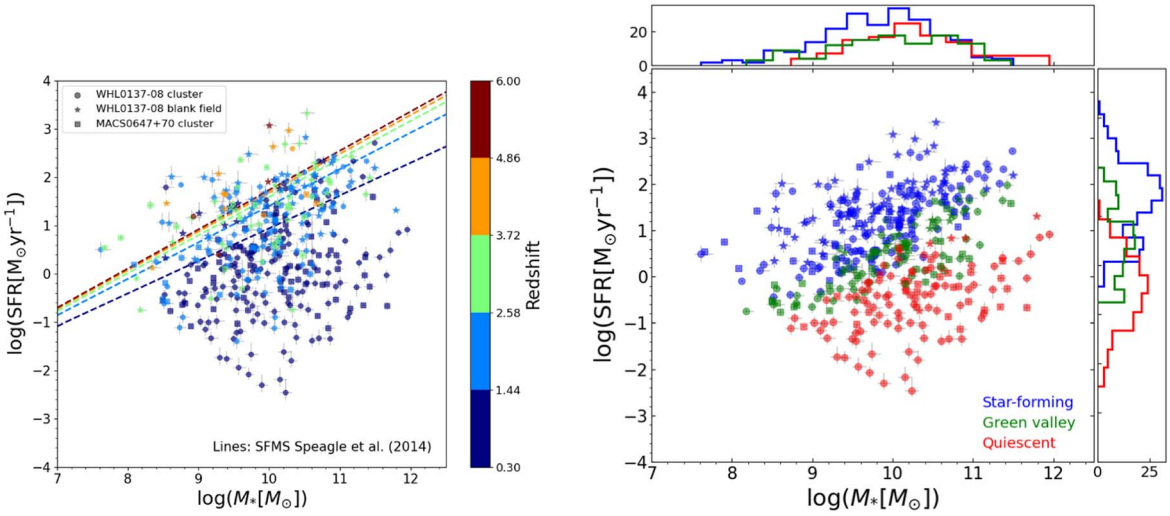

Figure 5. Left panel: integrated (i.e., global) M_* and SFR of our sample galaxies. Different symbols represent different fields where the galaxies are located, whereas the color coding represents redshift grouping. The dashed lines show the global SFMS relations at the median redshifts of the five redshift groups calculated using the prescription from Speagle et al. (2014). The lines are colored based on the redshift groups. Right panel: distribution of the star-forming, green-valley, and quiescent galaxies in our sample that are classified as having $\mathrm{SFR} > \mathrm{SFR_{MS}}(z,\ M_*) - 0.4$ dex, $\mathrm{SFR_{MS}}(z,\ M_*) - 0.4 \geqslant \mathrm{SFR} > \mathrm{SFR_{MS}}(z,\ M_*) - 1.0$ dex, and $\mathrm{SFR} \leqslant \mathrm{SFR_{MS}}(z, M_*) - 1.0$ dex, respectively. $\mathrm{SFR_{MS}}(z, M_*)$ is the SFMS ridge line that is calculated for the exact z and M_* of the individual galaxies.

using JWST NIRCam data (Hsiao et al. 2022; Pascale et al. 2022; Roberts-Borsani et al. 2022; Williams et al. 2022). We used this lens model constructed by Meena et al. (2023) for galaxies in the MACS 0647+70 field. We correct the M_* and SFR obtained from SED fitting for the lensing magnification by dividing them with μ. We also correct size or radius measurements by dividing them with μ_r.

4. Results

4.1. Integrated Properties

Before analyzing the spatially resolved properties of our sample galaxies, we first present their integrated (i.e., global) properties. To bring it into the context of the global demographics of galaxies, we plot our sample on the integrated SFMS diagram, as shown in the left panel of Figure 5. The integrated M_* and SFR of a galaxy are derived by summing up the values in pixels obtained from the spatially resolved SED fitting. Due to our limited sample, we plot all our galaxies on the SFMS diagram instead of dividing them into a number of redshift bins and examining the SFMS relation in each bin. This can cause a broad distribution as shown in the figure. Different symbols represent the fields where the galaxies are located (WHL 0137−08, blank field, and MACS 0647+70), whereas the color coding represents redshift grouping, where we divide the redshift range into five bins. The dashed lines show the SFMS relations at the median redshifts of the five redshift bins, calculated using the prescription from Speagle et al. (2014). The lines are colored based on the redshift groups.

We then classify our sample galaxies into star-forming, green-valley, and quiescent groups based on their positions with respect to the SFMS ridge line at the redshift of the galaxies. We define star-forming, green-valley, and quiescent galaxies as those having $\mathrm{SFR} > \mathrm{SFR_{MS}}(z,\ M_*) - 0.4$ dex, $\mathrm{SFR_{MS}}(z,\ M_*) - 0.4 \geqslant \mathrm{SFR} > \mathrm{SFR_{MS}}(z,\ M_*) - 1.0$ dex, and $\mathrm{SFR} \leqslant \mathrm{SFR_{MS}}(z, M_*) - 1.0$ dex, respectively, where $\mathrm{SFR_{MS}}(z, M_*)$ is the SFMS ridge line for the exact z and M_* of the individual galaxies. With this selection criteria, we have 219, 108, and 117 total numbers of the star-forming, green-valley, and quiescent galaxies from the three fields, respectively. We will use these classified samples throughout the analysis in this paper to investigate the differences in spatially resolved properties of galaxies in various evolutionary stages. The right panel of Figure 5 shows the distributions of these galaxy groups on the SFMS diagram.

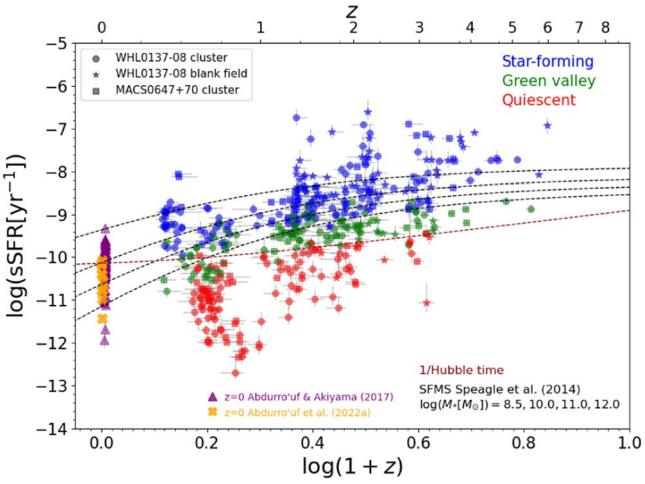

Figure 6. Evolution of the integrated specific SFR (sSFR) with redshift. The black dashed lines represent the sSFR evolution of SFMS galaxies with $M_* = 10^{8.5}$, 10^{10}, 10^{11}, and 10^{12} $M_\odot$ (decreasing normalization) as inferred from the normalization of the SFMS, calculated using the prescription from Speagle et al. (2014). The red dashed line represents $1/t_H$ where t_H is the Hubble time. Almost all our quiescent galaxies lie below this line, indicating that their mass-doubling timescale is longer than t_H.

To get a sense of how the global specific SFR ($\mathrm{sSFR} \equiv \mathrm{SFR}/M_*$) evolves with cosmic time in our sample galaxies, we plot the sSFR against redshift in Figure 6. We can see a clear trend of decreasing global sSFR with cosmic time and an increasing number of quiescent galaxies along the way. In our sample, quiescent galaxies start to emerge from $z \sim 3$, around 2 Gyr after the Big Bang. To compare our global sSFR trend with a similar trend from previous studies, we plot the sSFR(z) inferred from the SFMS normalization based on Speagle et al.

(2014) prescription. We calculate sSFR(z) with four M_* of $10^{8.5}$, 10^{10}, 10^{11}, and 10^{12} $M_\odot$ and show them in the figure as black dashed lines. We see an overall agreement between the evolutionary trend of sSFR in our sample and that expected based on the evolution of the SFMS normalization. We also show the global sSFR of local ($z \sim 0$) galaxies from Abdurro'uf & Akiyama (2017) and Abdurro'uf et al. (2022a, private communication), which were derived from spatially resolved SED fitting. Abdurro'uf & Akiyama (2017) analyzed 93 spiral galaxies at $0.01 < z < 0.02$ using imaging data from the GALEX (Morrissey et al. 2007) and SDSS (York et al. 2000) surveys. Abdurro'uf et al. (2022a) applied PIXEDFIT for analyzing 10 nearby galaxies using imaging data in more than 20 filters spanning the far-ultraviolet (FUV) to FIR.

Previous studies have classified passive galaxies using various methods. One of the methods is by comparing the Hubble time (t_H) with the mass-doubling time (i.e., the inverse of sSFR). Basically, this method defines quiescent galaxies as those having sSFR $< 1/t_H$. The red dashed line in Figure 6 represents $1/t_H$. We can see that our quiescent galaxies lie below this line, indicating that our classification method is consistent with that based on t_H.

4.2. Radial Profiles of the Stellar Population Properties

As we have shown the global properties of the sample galaxies and classified them into star-forming, green-valley, and quiescent groups, now we will analyze their spatially resolved properties. We start by presenting the radial profiles of the stellar population properties to get a sense of how the properties vary radially within the galaxies. To derive the radial profiles, first, we perform 2D single-component Sérsic fitting using GALFIT (Peng et al. 2002) on the F444W stamp image of each galaxy to get their ellipticities, position angles, and central coordinates. We then use this information to define elliptical annuli in the radial profile calculation. The radial profiles are derived from the 2D maps of properties obtained from the spatially resolved SED fitting by averaging the values of pixels within the annuli. Since galaxies have a wide range of sizes, we normalize the radius by the half-mass radius (R_e), which is the radius that covers half of the integrated M_*. We use a radial increment (δr) of $0.3R_e$. Thanks to the gravitational lensing effect, we can resolve many of our galaxies down to subkiloparsec scales (109 galaxies in our sample have delensed $R_e < 1$ kpc).

Figure 7 shows the radial profiles of the stellar-mass surface density (Σ_*). We divide the sample into five bins of redshift and four bins of M_* to see how the radial profiles vary with global M_* and cosmic time. Moreover, we indicate the star-forming, green-valley, and quiescent galaxies with different colors, in a similar way to Figure 6. For groups that contain at least five galaxies, we show average radial profiles with thick lines. Some interesting trends from Figure 7 are the following. At each redshift bin, more-massive galaxies tend to have higher normalization of $\Sigma_*(r)$ than less-massive ones, indicating that the excess in mass happens across the entire radius. Moreover, we also see that quiescent galaxies tend to have higher $\Sigma_*(r)$ normalization than the star-forming and green-valley galaxies in all redshifts. This is especially clear in the most-massive groups. It is also interesting to see that $\Sigma_*(r)$ profiles have a negative gradient (i.e., decreasing mass with increasing radius) in all redshift and mass bins, although the profiles seem to be shallower at higher redshifts.

To see how galaxies quench their star formation, specifically where in the galaxies the suppression of star formation first happens and how it progresses over cosmic time, we next analyze the radial profiles of sSFR. The radial profiles of sSFR are shown in Figure 8. As we can see from this figure, the sSFR radial profiles of the majority of our sample galaxies at $z \gtrsim 2.5$ are broadly flat, while they show more diversity in shape at lower redshifts. At $0.8 \lesssim z \lesssim 2.5$, star-forming galaxies in our sample tend to have a flat or centrally peaked sSFR(r), while quiescent galaxies tend to have centrally suppressed sSFR(r). On the other hand, green-valley galaxies in our sample seem to have broadly flat radial profiles up to $z \sim 1.0$, except in the most-massive group, where some of them show an sSFR suppression in their central regions. At lower redshifts, the majority of our sample galaxies have centrally suppressed sSFR(r). It is also interesting to see that the majority of star-forming galaxies at $0.8 \lesssim z \lesssim 2.5$ (in which the cosmic noon epoch is covered) have a centrally peaked sSFR(r). This central elevation of sSFR is not observed at higher redshifts.

Next, we analyze the radial profiles of the stellar population age to see how this quantity varies radially within our sample galaxies and investigate the underlying stellar population properties causing the diversity in the sSFR radial profiles. From our spatially resolved SED fitting, we obtain maps of the mass-weighted ages, which is the average age of stars in a stellar population as weighted by the stellar mass formed over the course of the star formation history. The age radial profiles are shown in Figure 9. As can be seen from this figure, there is a trend of increasing overall age of the stellar populations in galaxies over cosmic time, as indicated by the increasing normalization of the radial profiles with decreasing redshift. The star-forming galaxies that have a centrally peaked sSFR(r) at $0.8 \lesssim z \lesssim 2.5$ (possibly around the cosmic noon epoch) as shown in Figure 8 are likely in a phase of rapid star formation in their centers (i.e., a nuclear starburst; e.g., Dekel & Burkert 2014; Zolotov et al. 2015; Tacchella et al. 2016b; Tadaki et al. 2017), as indicated by the young stellar populations (age $\lesssim$100 Myr) in their central regions. At this epoch, green-valley and quiescent galaxies tend to have radially decreasing age profiles (i.e., a negative gradient). At $0.3 < z < 0.8$, low-mass galaxies ($\log(M_*/M_\odot) < 9.5$) in all stages of star formation have radially decreasing age radial profiles (i.e., a negative gradient). A similar trend still holds for star-forming and green-valley galaxies in the higher-mass group ($9.5 < \log(M_*/M_\odot) < 10.5$). On the other hand, quiescent galaxies at this epoch tend to have overall flat and old stellar populations across their entire radius, with higher normalization (i.e., older) than that of star-forming and green-valley galaxies.

4.3. Compactness of the Spatial Distributions of Stellar Mass and SFR

The centrally peaked sSFR(r) of star-forming galaxies at around the cosmic noon epoch indicates that they are likely undergoing a nuclear starburst that builds the bulge component, as has also been observed by previous studies (e.g., Tadaki et al. 2017; Kalita et al. 2022). The centrally suppressed sSFR (r) profiles that start to emerge in quiescent galaxies at around the same epoch can be caused by the cessation of star formation in the center and/or a matured bulge that has been formed in these galaxies. This trend provides a hint on how galaxies quench their star formation, which seems to progress in an

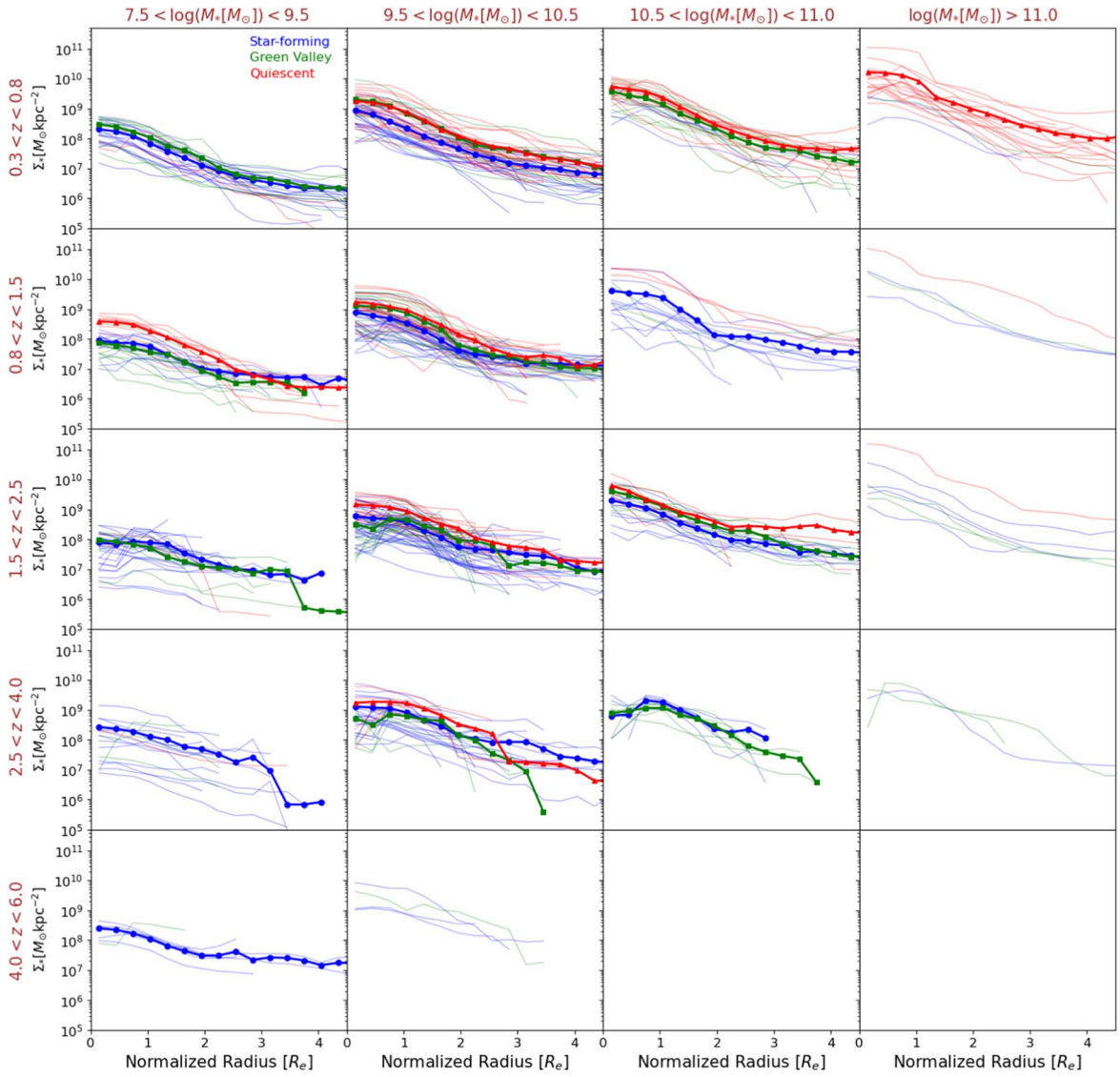

Figure 7. Radial profiles of the stellar-mass surface density (Σ_*). The sample galaxies are divided into four bins of global M_* and five bins of redshift. At each group, we further classify the galaxies into star-forming, green-valley, and quiescent groups and indicate them with different colors. For subgroups that contain at least five galaxies, we show average radial profiles with thick lines. At each redshift bin, more-massive galaxies tend to have higher $\Sigma_*(r)$ normalization than less-massive galaxies, indicating that the excess in mass happens across the galaxy region. Quiescent galaxies tend to have a higher $\Sigma_*(r)$ normalization than star-forming galaxies in all redshifts. This is especially clear in high-M_* bins.

inside-to-outside manner (i.e., quenching starts from the center and then propagates outward). At the same time, this trend may indicate that galaxies build their central regions first, forming a mature bulge, and then subsequently assemble their disk through star formation (i.e., inside-out growth). To further investigate this, next we compare the compactness of the spatial distributions of M_* and SFR by means of the half-mass and half-SFR radii.

We compare the half-mass radius and the half-SFR radius in Figure 10. The half-SFR radius is a radius (measured along the elliptical semimajor axis) that covers half of the total SFR. To compare the distributions of our star-forming and quiescent galaxies on this diagram, we plot the density contours. As can be seen from this figure, star-forming galaxies broadly follow the one-to-one line, whereas quiescent galaxies are in excess above the line. This means that in quiescent galaxies, the spatial distribution of SFR is more extended than that of stellar mass, indicating that star formation is ongoing in the disk and less active in the central region. It is also possible that a massive bulge might have been formed in the centers, making a more compact stellar-mass distribution. On the other hand, star-forming galaxies are equally distributed. Some star-forming galaxies have spatially more compact star formation distribution than the stellar mass (i.e., below the one-to-one line), which indicates that active star formation happens at their centers. On the other hand, in the star-forming galaxies that have extended star formation (i.e., above the one-to-one line), the bulge might have been built and active star formation is now progressing outward and building the disk.

It has been known that galaxy size correlates with global M_* for galaxies out to at least $z \sim 3$ (i.e., the size–mass relation; e.g., Shen et al. 2003; Morishita et al. 2014; van der Wel et al. 2014; Yang et al. 2021). However, most of the previous studies rely on galaxy half-light radii as a measure of galaxy size. Since mass-to-light ratios are not constant across a galaxy's region but instead have a gradient, the half-light radii are not a

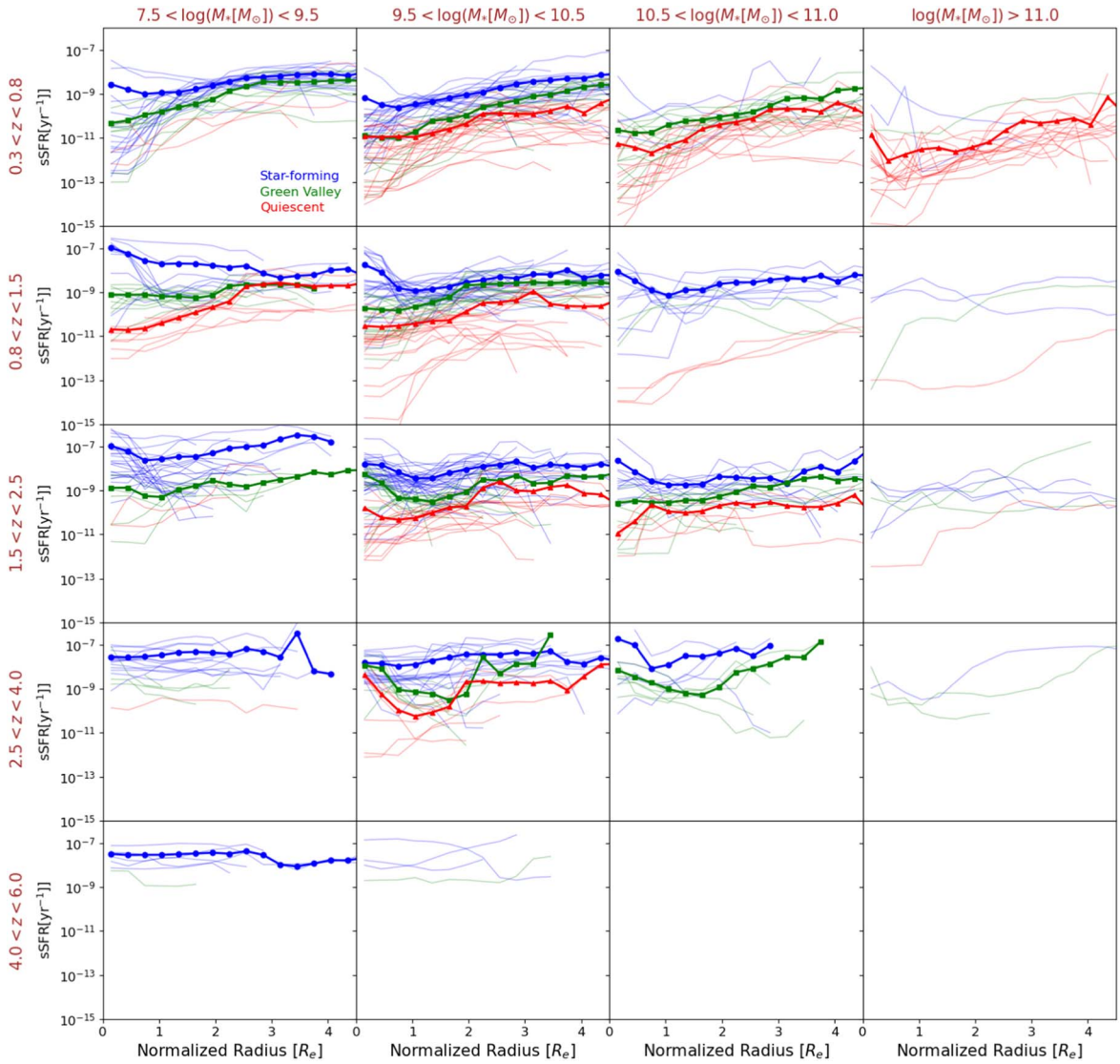

Figure 8. Similar to Figure 7 but for radial profiles of sSFR. At $z \gtrsim 2.5$, our sample galaxies tend to have a broadly flat sSFR (r), while at the lower redshifts, they show more diversity in shape. At $0.8 \lesssim z \lesssim 2.5$, the majority of star-forming galaxies have an elevation of sSFR in their central regions, while they tend to have centrally suppressed sSFR radial profiles at lower redshifts. On the other hand, quiescent galaxies in our sample tend to have centrally suppressed sSFR radial profiles since $z \sim 1.5$.

direct probe of the underlying stellar-mass profiles. Therefore, it is expected that the half-mass and half-light radii are different. The difference in size as probed by light and mass profiles in galaxies out to $z \sim 2.5$ has been investigated by previous studies (e.g., Suess et al. 2019).

Now, we check how the half-mass and half-SFR radii correlate with the integrated M_* in our sample galaxies. We show the correlations in Figure 11. Overall, we see that both half-mass and half-SFR radii increase as increasing integrated M_*. However, we observe a difference in how star-forming and quiescent galaxies are distributed in the two correlations. In the top panel, we can see that star-forming galaxies tend to have a larger half-mass radius than quiescent galaxies in all masses. On the other hand, as can be seen from the bottom panel, there is no clear difference between the star-forming and quiescent galaxies in terms of the half-SFR radius, although star-forming galaxies tend to have a wider range of half-SFR radius than quiescent galaxies.

In agreement with the trend we observe here, previous studies using half-light radii also found that star-forming galaxies are larger than quiescent galaxies in all M_* (van der Wel et al. 2014). However, when the half-mass radius is used, the normalization of the relation decreases, and the slope as well becomes shallower (Suess et al. 2019). We do not intend to measure the slope and normalization of our size–mass relations because of the limited sample. Ideally, we need a large sample of galaxies and divide them into some redshift bins. In this work, we combine all galaxies in our sample despite the fact that they are located in a wide range of redshifts.

4.4. Central Stellar-mass Surface Density

We have observed that quiescent galaxies have a smaller half-mass radius than star-forming galaxies. The quiescent galaxies at $z \lesssim 2.5$ also have centrally suppressed sSFR radial profiles. The compactness of quiescent galaxies can be caused by the massive bulge that has been formed in their centers. This massive bulge may also be the reason behind the central suppression of sSFR. Therefore, here we investigate the

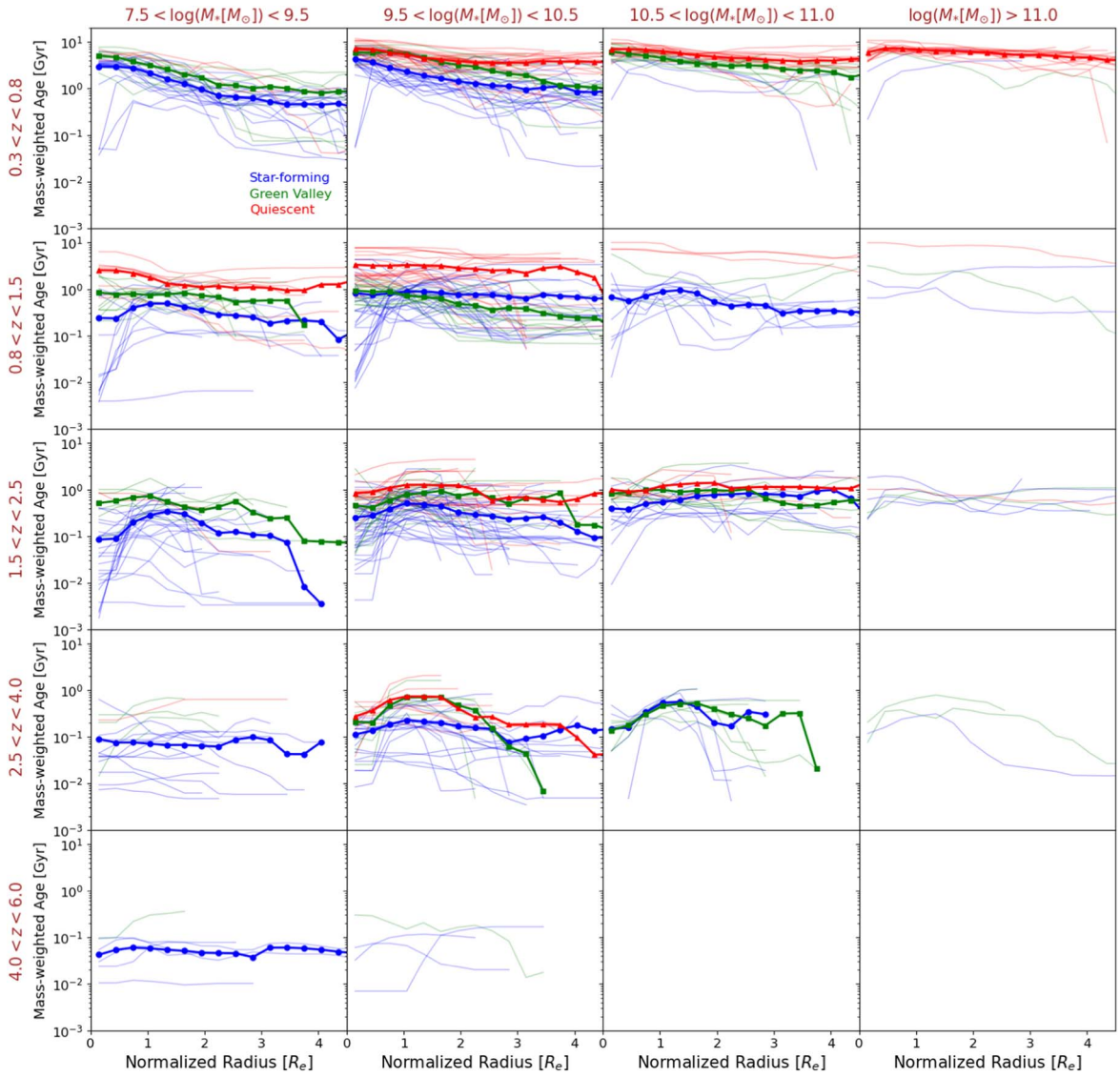

Figure 9. Similar to Figure 7 but for radial profiles of the stellar population age. There is a trend of increasing the overall age of the stellar populations in galaxies over cosmic time. At $0.8 \lesssim z \lesssim 2.5$ (possibly around the cosmic noon epoch), a large fraction of our star-forming galaxies have a centrally suppressed age radial profile. Those galaxies have centrally peaked sSFR radial profiles as shown in Figure 8. These trends indicate that they are likely to have an ongoing nuclear starburst event.

stellar-mass surface density in the central 1 kpc radius ($\Sigma_{*,1\mathrm{kpc}}$) of our sample galaxies.

Figure 12 shows a relationship between the integrated M_* and $\Sigma_{*,1\mathrm{kpc}}$. A tight relationship is evidenced by this figure, which indicates that $\Sigma_{*,1\mathrm{kpc}}$ grows hand in hand with the integrated M_* of the galaxies. We fit the relation involving all galaxies in our sample with a linear function (in logarithmic scale) using the orthogonal distance regression (ODR) method and find that the relationship has a scatter of 0.38 dex. The best-fit linear function (with a slope of 1.10 and zero-point of -2.33) is shown with the purple dashed line. It is interesting to see that quiescent galaxies mostly reside in a tight locus at the top of the relation. This trend indicates that quiescent galaxies tend to be massive and have a massive central stellar-mass density, perhaps associated with a bulge that has been formed in these galaxies. This massive central component might in part cause the more compact (i.e., smaller half-mass radius) size of quiescent galaxies compared to the star-forming galaxies. In Section 5.1, we will discuss further how this central stellar-mass density evolves with redshift and correlates with star formation in the inner and outer regions of the galaxies.

A similar relationship has also been observed by previous studies in galaxies at $z \lesssim 3$ (e.g., Fang et al. 2013; Tacchella et al. 2015; Barro et al. 2017). Using a larger sample than ours, they also found that quiescent galaxies occupy a tight locus on top of the overall relationship with all galaxies. The relation involving only quiescent galaxies has a shallower slope than that with star-forming galaxies only. The black and red dashed lines are the best fit to the M_*–$\Sigma_{*,1\mathrm{kpc}}$ relation of $z \sim 0$ passive galaxies reported by Fang et al. (2013) and Tacchella et al. (2015), respectively, whereas the blue line is the best fit to the relation of $z \sim 0$ star-forming galaxies from Tacchella et al. (2015). In our result, we also see a slight bending at the tip of the distribution of quiescent galaxies, as can be seen from the density contour. It is interesting to see the consistency between the M_*–$\Sigma_{*,1\mathrm{kpc}}$ relation from our study and that from the literature despite the fact that our sample galaxies cover a wider redshift range ($0.3 < z < 6.0$). It suggests that this relation might be universal and galaxies evolve along this tight relation.

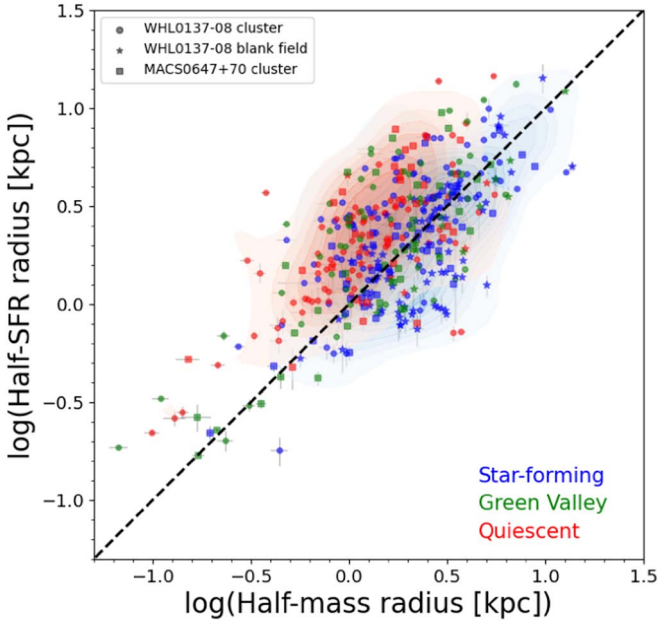

Figure 10. Comparison between the half-mass radius and half-SFR radius. The overall symbols in this figure are the same as those in Figure 6. The red and blue contours show the number densities of the star-forming and quiescent galaxies. The majority of quiescent galaxies in our sample have spatially more extended star formation distribution than the stellar mass. Star-forming galaxies are equally distributed on the diagram. In star-forming galaxies with a compact SFR distribution (i.e., below the one-to-one line), an active star formation happens in the central region. On the other hand, in star-forming galaxies with less compact SFR distribution, a bulge might have been built and active star formation is now progressing outward, building the disk.

5. Discussions

5.1. How Do Galaxies Grow and Quench over Cosmic Time?

In this section, we exploit our results to try to infer how galaxies assemble their structures and eventually cease their star formation activities over the course of their life. In particular, we are interested in investigating how the processes of stellar-mass buildup and quenching were propagating within the galaxies. Based on the models of the hierarchical galaxy formation paradigm, within the framework of the ΛCDM cosmology, galaxies are predicted to build their structures over cosmic time in an inside-out manner, where the central component was built first and subsequently the disk structure is assembled gradually over time (e.g., Cole et al. 2000; van den Bosch 2002; Aumer & White 2013). This assembly process happens through the series of gas accretions via mergers and filamentary accretion through the cosmic web.

In a gas-rich merger, gas can fall rapidly into the center of the gravitational potential, causing compaction of gas that eventually triggers a nuclear starburst event (e.g., Dekel & Burkert 2014). Other smoother gas streams can also lead to central gas compaction, e.g., counterrotating streams and low-angular-momentum recycled gas. Based on the zoom-in cosmological hydrodynamical simulations, this wet compaction event is predicted to typically occur in $\sim 10^{9.5} M_{\odot}$ galaxies at $z \sim 2$–4 (e.g., Zolotov et al. 2015; Tacchella et al. 2016a, 2016b). During this event, the star formation at the center is very intense, which converts massive gas concentration rapidly into stars (i.e., with a short depletion time). This process depletes the gas in galaxies and makes the SFR decline. However, the gas compaction event can occur multiple times in high-redshift galaxies, causing an up and down of their SFRs. This could appear as an oscillation around the SFMS ridge line. The gas compaction and nuclear starburst processes can build a massive bulge in the centers of the galaxies (Tacchella et al. 2016a, 2016b). Subsequently, galaxies can reach full quenching when the timescale of gas replenishment in the disk is longer than the timescale of gas depletion by star formation. This is more likely to happen at lower redshifts when the cosmological gas accretion rate is low and especially so in a hot halo above the critical halo mass of $\sim 10^{11.5} M_{\odot}$ (Birnboim & Dekel 2003; Kereš et al. 2005; Dekel & Birnboim 2006). In general, an emerging picture from the above scenarios is that galaxies build their structures and quench their star formation in an inside-out manner.

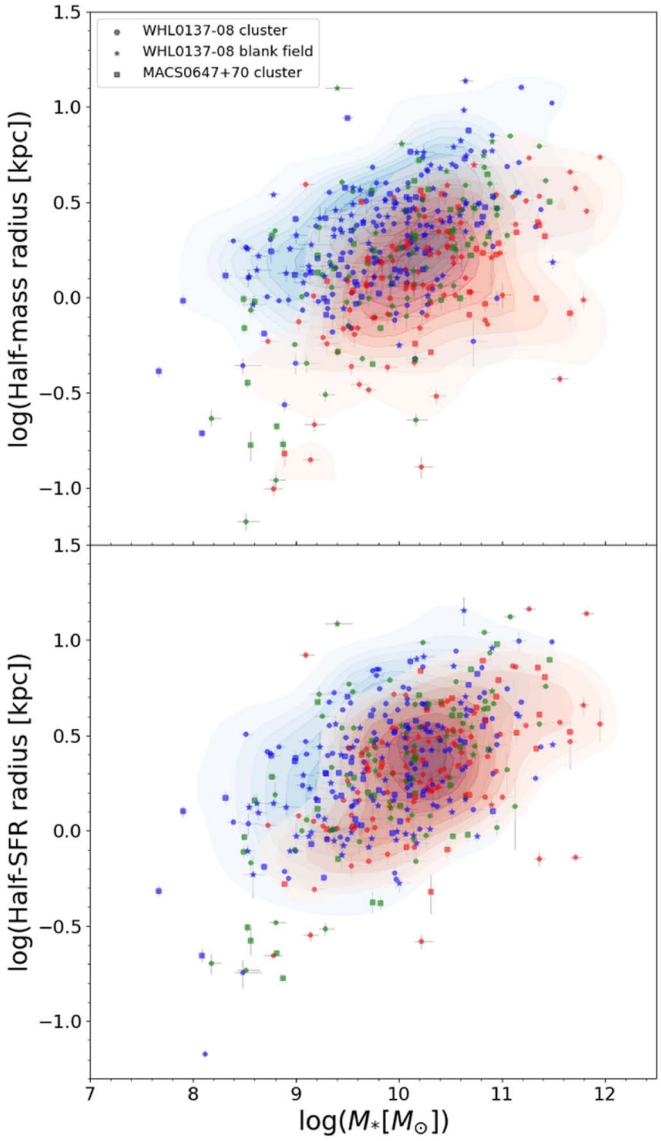

Figure 11. The half-mass (top panel) and half-SFR (bottom panel) radii as a function of integrated M_*. The overall symbols in this figure are the same as those in Figure 10. The half-mass radius is defined as the radius that covers half of the total M_*, while the half-SFR radius is the radius covering half of the total SFR. Both half-mass and half-SFR radii increase with increasing M_*. The M_* vs. half-mass radius diagram shows that overall, the star-forming galaxies tend to have a larger size than quiescent galaxies. However, there is no clear difference between the two groups in terms of the size of the SFR distribution.

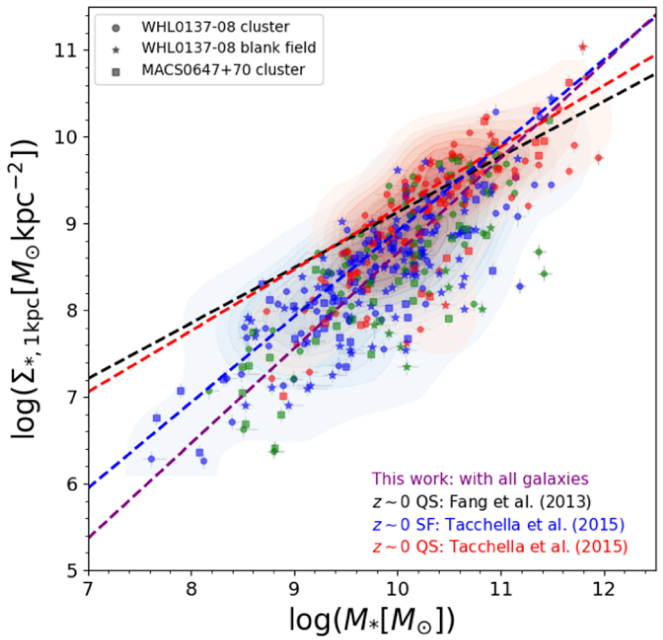

Figure 12. A tight relationship between the integrated M_* and stellar-mass surface density within the central 1 kpc radius ($\Sigma_{*,1\mathrm{kpc}}$). The overall symbols in this figure are the same as those in Figure 10. This relation indicates that $\Sigma_{*,1\mathrm{kpc}}$ grows hand in hand with the integrated M_*. The quiescent galaxies mostly reside in the top locus of the relation, indicating that they tend to be massive and have a massive spheroid in their centers. The purple dashed line is the best-fit linear function to our sample galaxies, which has a slope of 1.10, zero-point of −2.33, and scatter of 0.38 dex. The black and red dashed lines are the best fit to the same relation found in $z \sim 0$ passive galaxies reported by Fang et al. (2013) and Tacchella et al. (2015), respectively, whereas the blue line is the best fit to the relation of $z \sim 0$ star-forming galaxies from Tacchella et al. (2015).

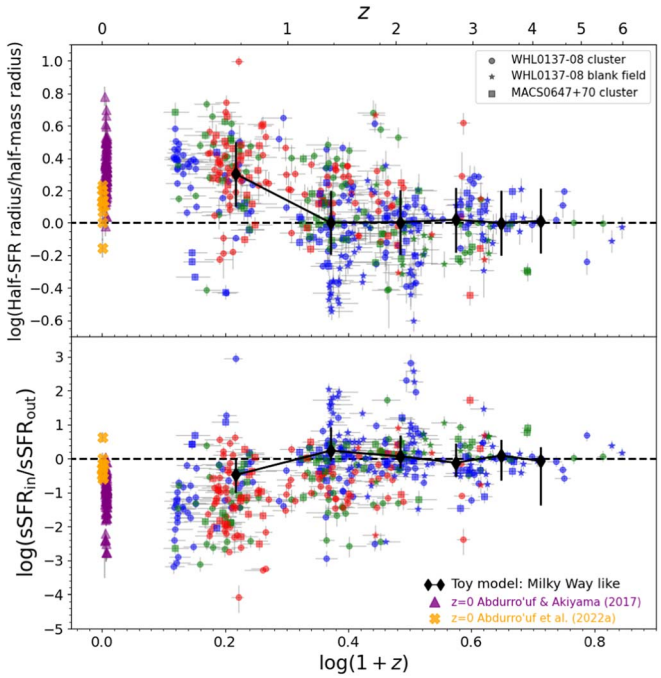

Figure 13. Evolution of the ratio between the half-SFR and half-mass radii (top panel) and the ratio between the sSFR inside and outside of the half-mass radius (bottom panel). The overall symbols and color coding are the same as those in the right panel of Figure 5. The profiles shown with black diamond symbols represent an expectation from a toy empirical model for the evolution of the Milky Way analogs. For comparison, we also show the trends observed in local spiral galaxies from Abdurro'uf & Akiyama (2017) and Abdurro'uf et al. (2022a). At $z \gtrsim 3.5$, the two ratios are close to unity, indicating a similar mass-doubling time across the galaxy's region. At $1.5 \lesssim z \lesssim 2.5$, many star-forming galaxies have a compact star formation ($R_{e,\mathrm{SFR}}/R_e$ as low as $\sim$−0.5 dex and $\mathrm{sSFR_{in}}/\mathrm{sSFR_{out}}$ up to $\sim$3 dex). The majority of the green-valley and quiescent galaxies at this epoch have $R_{e,\mathrm{SFR}}/R_e > 1$ and $\mathrm{sSFR_{in}}/\mathrm{sSFR_{out}} < 1$. At a later epoch ($z \lesssim 1.5$), the majority of quiescent, green-valley, and star-forming galaxies have extended SFR distributions and centrally suppressed sSFR. Overall, these trends point toward the inside-out growth and quenching scenario.

Next, we will exploit our observational results to find indications of the above model predictions. We note that our current sample is limited, which may cause some biases in our interpretations. More information from multiwavelength observations is needed for a more comprehensive study on this, including maps of the gas mass and their kinematics, which can be obtained from radio and integral field spectroscopy observations. We leave this for future work.

First, we examine the evolution of the ratio between the half-SFR and half-mass radii and the ratio between the sSFR in the inner ($\mathrm{sSFR_{in}}$) and outer ($\mathrm{sSFR_{out}}$) regions of the galaxies. We show the evolution of these quantities in Figure 13. The $\mathrm{sSFR_{in}}$ and $\mathrm{sSFR_{out}}$ are defined as the total sSFR inside and outside of the half-mass radius, respectively. In the study of galaxy evolution, we face the fact that we observe galaxies at a certain cosmic time. In other words, the galaxies across the wide redshift that we observe here are not necessarily connected evolutionarily (i.e., they may not be progenitor–descendant pairs), which makes it difficult to interpret an evolutionary trend from our study. Previous studies have tried to connect galaxies using an M_* growth function ($M_*(z)$) derived from the stellar-mass function assuming a constant number density (e.g., van Dokkum et al. 2010, 2013). To try to connect galaxies in our sample and infer some evolutionary trends from their properties, we use the $M_*(z)$ from van Dokkum et al. (2013; Equation (1) therein), which was designed to trace the evolution of Milky Way analogs (i.e., having $M_* = 5 \times 10^{10} M_\odot$ at $z = 0$). We bin the redshift with a width of 0.7. By using the $M_*(z)$ function, we then choose galaxies that fall within±0.35 dex in M_* at each redshift bin. Our model only extends up to $z = 4.5$ because there are no low-mass galaxies selected beyond it in our sample. This can be caused by a bias in our sample selection (see Section 2.2). This toy empirical model is only intended as a reference in interpreting observational trends. We show the evolutionary trends of this toy model with black diamond symbols. For comparison, we also show the trends observed in local spiral galaxies, as inferred from the data analyzed by Abdurro'uf & Akiyama (2017) and Abdurro'uf et al. (2022a, private communication).

The ratio between the half-SFR and half-mass radii ($R_{e,\mathrm{SFR}}/R_e$) tells us about the relative extent of the SFR distribution compared to the stellar-mass distribution. A ratio $R_{e,\mathrm{SFR}}/R_e < 1$ implies a more compact SFR distribution than the stellar mass, whereas $R_{e,\mathrm{SFR}}/R_e > 1$ implies a more compact mass distribution than star formation. $R_{e,\mathrm{SFR}}/R_e << 1$ may indicate an ongoing nuclear starburst, while $R_{e,\mathrm{SFR}}/R_e >> 1$ indicates that a massive bulge has been built in the galaxies. From Figure 13, we can see that from an early epoch up to $z \sim 3.5$, the two ratios are close to unity, indicating a similar mass-doubling time across the galaxy's region. In our sample, we only have star-forming and green-valley galaxies at this epoch. Quiescent galaxies emerge from $z \sim 3$ in our sample, and we start to see more dispersion in the two ratios at this later epoch. At $1.5 \lesssim z \lesssim 2.5$, we see a large fraction of our

star-forming galaxies have a compact star formation with $R_{e,\mathrm{SFR}}/R_e$ as low as ~-0.5 dex and centrally peaked sSFR with $\mathrm{sSFR_{in}}/\mathrm{sSFR_{out}}$ of up to $\sim$3 dex. In contrast to this, the majority of green-valley and quiescent galaxies at this epoch have $R_{e,\mathrm{SFR}}/R_e>1$ and $\mathrm{sSFR_{in}}/\mathrm{sSFR_{out}}<1$. At a later epoch ($z\lesssim 1.5$), the majority of quiescent, green-valley, and star-forming galaxies have extended SFR distributions and centrally suppressed sSFR. The toy model has constant ratios of $\sim$1 from the early epoch up to $z\sim 1.5$ after which its sSFR declines and the SFR distribution becomes more extended. There is an indication that its $\mathrm{sSFR_{in}}/\mathrm{sSFR_{out}}$ actually increases a little bit above 1 at $z\sim 1.5$.

The trends observed at $z\sim 0$ indicate that local spiral galaxies have overall extended SFR distributions and centrally suppressed sSFR radial profiles. These trends agree with the scenarios inferred from our results in the current work and provide a nice extension to our results toward low redshift, complementing the general picture.

Overall, the above trend agrees with the inside-out growth and quenching scenarios. In early cosmic time, galaxies get steady gas accretion for star formation but they have yet to form a bulge, and the star formation is likely distributed evenly across their regions. At $z\sim 2$, which coincides with the peak epoch of the cosmic SFRD and perhaps the cosmic gas accretion (Madau & Dickinson 2014), star-forming galaxies in our sample may experience gas compaction events that later build bulge in their centers. After that, quenching might have been started in their central regions, but star formation is still active in the disk, further building the disk. In addition to in situ star formation, minor mergers can also contribute to the buildup of stellar mass in the disk and grow the galaxy size.

5.2. The Buildup of the Central Stellar-mass Density over Cosmic Time

As we have seen in Section 4.4, our sample galaxies exhibit a tight relationship between the global M_* and $\Sigma_{*,1\mathrm{kpc}}$. $\Sigma_{*,1\mathrm{kpc}}$ is a good indicator for quiescent galaxies because they form a rather distinct sequence at the tip of the overall M_*–$\Sigma_{*,1\mathrm{kpc}}$ relation and have a shallower slope. Here we discuss the evolution of $\Sigma_{*,1\mathrm{kpc}}$ with redshift to see how the central bulge is built over cosmic time in our sample galaxies. As $\Sigma_{*,1\mathrm{kpc}}$ develops over time, it is also interesting to analyze how sSFR at the central 1 kpc evolves following the development of $\Sigma_{*,1\mathrm{kpc}}$. The evolution of these two quantities is shown in Figure 14. As we can see from this figure, $\Sigma_{*,1\mathrm{kpc}}$ tends to increase with cosmic time, whereas $\mathrm{sSFR_{1kpc}}$ declines with cosmic time. The quiescent galaxies tend to have higher $\Sigma_{*,1\mathrm{kpc}}$ and lower $\mathrm{sSFR_{1kpc}}$ in all redshifts. The $\mathrm{sSFR_{1kpc}}$ of quiescent and green-valley galaxies tend to be declined more rapidly than that of star-forming galaxies. Interestingly, the overall $\mathrm{sSFR_{1kpc}}$ of our star-forming galaxies does not decline much from $z=6$ up to $z\sim 1.5$. There is an indication that the $\mathrm{sSFR_{1kpc}}$ of some star-forming galaxies even increases at $1.5\lesssim z\lesssim 2.5$.

The black profiles show the expected evolution of Milky Way analogs based on our toy model derived in Section 5.1. Its $\Sigma_{*,1\mathrm{kpc}}$ increases by $\sim$2 mag over $0.5\lesssim z\lesssim 4.5$, while its $\mathrm{sSFR_{1kpc}}$ decreases significantly ($\sim$3.7 mag) over the same period. This implies that the central SFR within 1 kpc also decreases with time. At $1.5\lesssim z\lesssim 2.5$, the $\mathrm{sSFR_{1kpc}}$ of this model seems to be constant. In addition to our toy model, we also compare our observational trend with the predictions from the VELA zoom-in cosmological hydrodynamical simulations

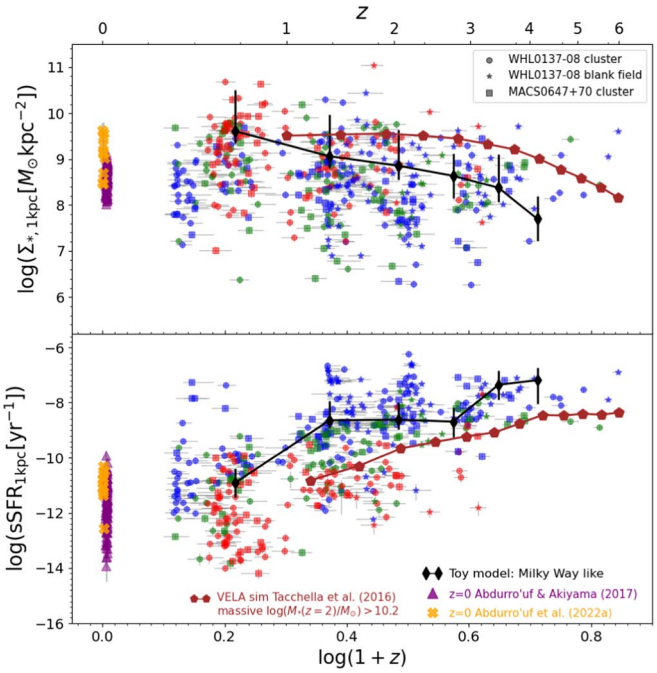

Figure 14. The buildup of the stellar-mass density at the central 1 kpc ($\Sigma_{*,1\mathrm{kpc}}$) over cosmic time (top panel) and the evolution of sSFR at the central 1 kpc ($\mathrm{sSFR_{1kpc}}$; bottom panel). The profiles shown with black diamond symbols represent an expectation from a toy empirical model for the evolution of the Milky Way analogs, whereas the red pentagon symbols show a prediction from the zoom-in cosmological hydrodynamical simulations by Tacchella et al. (2016a) for the evolution of massive galaxies ($\log(M_*(z=2)/M_\odot)>10.2$).

(Ceverino et al. 2014; Zolotov et al. 2015) that were analyzed by Tacchella et al. (2016a). These predictions, which are shown in red profiles, are obtained by averaging the evolutionary trends of relatively massive galaxies in the simulations that have $\log(M_*/M_\odot)=10.2$ at $z=2$. This simulation was run over $1<z<7$. The $\Sigma_{*,1\mathrm{kpc}}$ and $\mathrm{sSFR_{1kpc}}$ predicted from the cosmological simulation at $z\sim 6$ are in good agreement with our observations. The evolution of the $\Sigma_{*,1\mathrm{kpc}}$ and $\mathrm{sSFR_{1kpc}}$ from the simulation might be consistent with the evolution of the progenitors of local massive quiescent galaxies, as implied from our observations. However, there is an excess of $\Sigma_{*,1\mathrm{kpc}}$ at $z\sim 0.5$ quiescent galaxies compared to the simulation. Those galaxies are likely members of the WHL 0137−08 or MACS 0647+70 clusters. In clusters, galaxies could accrete more mass through mergers, which can result in a denser central mass density.

The trends at $z\sim 0$ from Abdurro'uf & Akiyama (2017) and Abdurro'uf et al. (2022a) provide a good extension for our results in the current work. They overall agree with the picture of increasing $\Sigma_{*,1\mathrm{kpc}}$ and decreasing $\mathrm{sSFR_{1kpc}}$ with cosmic time. However, we also see a lower $\Sigma_{*,1\mathrm{kpc}}$ in the local spiral galaxies than in the quiescent galaxies at $z\sim 0.5$ that are possibly the cluster members. If we ignore these galaxies and assume that the $\Sigma_{*,1\mathrm{kpc}}$ trend from the VELA simulation will evolve to have a similar value as those of the observed $\Sigma_{*,1\mathrm{kpc}}$ of local galaxies (which is likely, given its shallow slope at $z\sim 1$), we see a possible saturation of central mass density in galaxies.

Next, we compare the effects of $\Sigma_{*,1\mathrm{kpc}}$ and the global M_* on $\mathrm{sSFR_{in}}/\mathrm{sSFR_{out}}$. We show the $\Sigma_{*,1\mathrm{kpc}}$–$\mathrm{sSFR_{in}}/\mathrm{sSFR_{out}}$ and M_*–$\mathrm{sSFR_{in}}/\mathrm{sSFR_{out}}$ relations in Figure 15. We can see from this figure that $\mathrm{sSFR_{in}}/\mathrm{sSFR_{out}}$ is correlated with both $\Sigma_{*,1\mathrm{kpc}}$

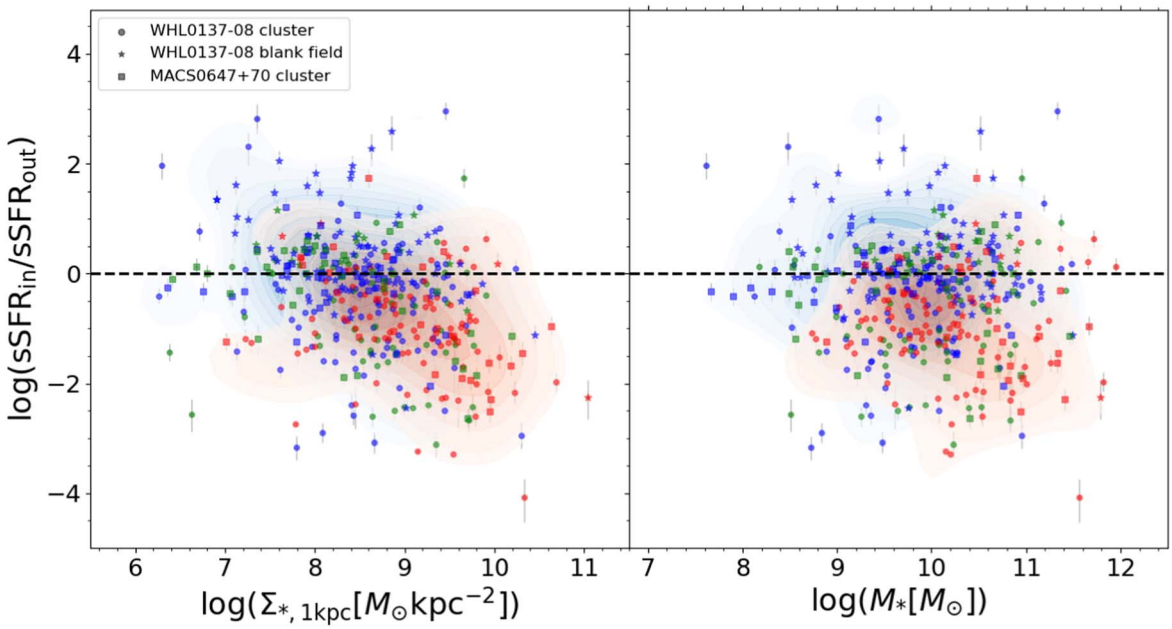

Figure 15. The $\mathrm{sSFR_{in}/sSFR_{out}}$ ratio as a function of the central mass density (left panel) and global M_*(right panel). The overall symbols in this figure are the same as those in Figure 10. Galaxies that are massive and have high $\Sigma_{*,1kpc}$ tend to have centrally suppressed sSFR profiles. This trend is predominantly observed in quiescent galaxies. The M_*–$\mathrm{sSFR_{in}/sSFR_{out}}$ relation seems to be broader and less significant compared to M_*–$\mathrm{sSFR_{in}/sSFR_{out}}$, indicating that $\Sigma_{*,1kpc}$ is more influential in driving $\mathrm{sSFR_{in}/sSFR_{out}}$ than global M_*.

and the global M_* such that increasing $\Sigma_{*,1kpc}$ and M_* correspond to a steeper sSFR decline in the central regions. However, the M_*–$\mathrm{sSFR_{in}/sSFR_{out}}$ relation seems to be broader and less significant compared to M_*–$\mathrm{sSFR_{in}/sSFR_{out}}$, indicating that $\Sigma_{*,1kpc}$ is more influential in driving $\mathrm{sSFR_{in}/sSFR_{out}}$ than the global M_*. The majority of those that have central sSFR suppression are the quiescent and green-valley galaxies, whereas a significant fraction of star-forming galaxies have broadly flat or centrally peaked sSFR radial profiles (i.e., a negative gradient). This further suggests that $\Sigma_{*,1kpc}$ is a good predictor for quiescent galaxies, which agrees with previous studies (e.g., Cheung et al. 2012; Fang et al. 2013; Barro et al. 2017; Jung et al. 2017; Whitaker et al. 2017; Bluck et al. 2022).

Some physical mechanisms for the quenching in galaxies have been proposed, including stellar feedback (e.g., Dekel & Silk 1986; Murray et al. 2005), AGN feedback (e.g., Di Matteo et al. 2005; Croton et al. 2006; Ciotti & Ostriker 2007; Cattaneo et al. 2009), kinematic stabilization of gas in the disk by a massive bulge (e.g., Martig et al. 2009; Genzel et al. 2014), and long-term suppression of gas supply due to the virial shock heating by the dark matter halo when it has reached a threshold mass of $\sim 10^{11.5} M_\odot$ (e.g., Birnboim & Dekel 2003; Dekel & Birnboim 2006; Kereš et al. 2009). The inside-out quenching observed in this work seems to agree with the AGN feedback scenario, as has also been suggested by previous spatially resolved studies of galaxies at $z \lesssim 2$ (e.g., Nelson et al. 2021; Bluck et al. 2022). The feedback from AGNs can expel or heat up gas, which then causes the suppression of star formation in at least the central region of the galaxies. The feedback strength must scale with the mass of the supermassive black hole (SMBH), which has been known to correlate tightly with the bulge mass (e.g., Häring & Rix 2004; Schutte et al. 2019). This is overall in line with our results, which show that quiescent galaxies tend to have a centrally suppressed sSFR and high central mass density. However, a more in-depth study is needed to further investigate this. Ideally, we need multiwavelength data sets that allow us to identify AGNs and measure the strength of its feedback, which we have not had in this study.

6. Summary and Conclusions

We perform spatially resolved SED fitting on 444 galaxies at $0.3 < z < 6.0$ in two clusters (WHL 0137−08 and MACS 0647 +70) and a blank field using imaging data from JWST and HST in up to 13 bands. We use PIXEDFIT throughout the analysis. This software can simultaneously perform image processing, pixel binning, and spatially resolved SED fitting. By using the maps of spatially resolved stellar population properties (on kiloparsec scales) obtained from this analysis, we investigate how galaxies grow their structures and quench their star formation activities across cosmic time. Overall, our key results are summarized in the following:

1. The normalization of the stellar-mass surface density radial profiles ($\Sigma_{*,1kpc}(r)$) increases with increasing cosmic time and global M_*. At each redshift, quiescent galaxies tend to have a higher $\Sigma_{*,1kpc}$ across the entire radius than green-valley and star-forming galaxies. The sSFR radial profiles (sSFR(r)) show more variations across redshift and global M_*. The sSFR(r) is broadly flat at $2.5 \lesssim z \lesssim 6.0$ in all galaxies, indicating a similar mass-doubling time across the entire radius. At $0.8 \lesssim z \lesssim 2.5$, less-massive ($\log(M_*/M_\odot) < 11.0$) star-forming galaxies have flat or centrally peaked sSFR (r), whereas the majority of quiescent galaxies have a centrally suppressed sSFR(r). At lower redshift ($z < 0.8$), almost all galaxies (regardless of M_* and star formation stage) have centrally suppressed sSFR(r). The radial profiles of stellar ages show that those galaxies with a centrally peaked sSFR(r) at $0.8 \lesssim z \lesssim 2.5$ have very young stellar populations in their central regions, indicating an ongoing nuclear starburst.

2. The majority of quiescent galaxies have a half-SFR radius larger than the half-mass radius, indicating that they have an extended spatial distribution of the SFR and a compact distribution of stellar mass. In contrast, some star-forming galaxies, especially at high redshifts, have a half-SFR radius roughly similar to or smaller than the half-mass radius, whereas those at low redshifts have a half-SFR radius larger than the half-mass radius. The half-mass radius of the star-forming galaxies is on average larger than the quiescent galaxies in all global M_*.
3. We observe a tight correlation between the global M_* and stellar-mass density at the central 1 kpc radius ($\Sigma_{*,1\mathrm{kpc}}$) with 0.38 dex, indicating that galaxies grow their central mass density hand in hand with their global M_*. The quiescent galaxies reside in a sequence at the tip of the overall relationship and have a shallower slope. This trend indicates that $\Sigma_{*,1\mathrm{kpc}}$ is a good predictor of quenching, where passive galaxies tend to have higher $\Sigma_{*,1\mathrm{kpc}}$ and global M_*. The shallower slope of M_*–$\Sigma_{*,1\mathrm{kpc}}$ in quiescent galaxies suggests that their central mass density has reached a saturation point.
4. We investigate the evolution of the $R_{e,\mathrm{SFR}}/R_e$ and $\mathrm{sSFR_{in}}/\mathrm{sSFR_{out}}$ ratios with redshift to try to understand how galaxies grow their structures and quench their star formations over cosmic time. We find that the ratios are close to unity from the early epoch up to $z \sim 3.5$, and the ratios start to deviate from unity since then. At $1.5 \lesssim z \lesssim 2.5$, a fraction of our star-forming sample has a low $R_{e,\mathrm{SFR}}/R_e$ and high $\mathrm{sSFR_{in}}/\mathrm{sSFR_{out}}$, indicating that they may be experiencing a nuclear starburst. At the later epoch, most of our sample galaxies, especially quiescent and green valley, have a high $R_{e,\mathrm{SFR}}/R_e$ and low $\mathrm{sSFR_{in}}/\mathrm{sSFR_{out}}$, suggesting that massive bulges might have been formed in these galaxies and the star formation has been quenched in their central regions.
5. We also investigate the evolution of $\Sigma_{*,1\mathrm{kpc}}$ and sSFR at the central 1 kpc ($\mathrm{sSFR_{1kpc}}$). In general, we see an increasing $\Sigma_{*,1\mathrm{kpc}}$ and decreasing $\mathrm{sSFR_{1kpc}}$ with cosmic time, indicating the buildup of the central bulge component and the quenching process in the central region of the galaxies. We also find that quiescent galaxies tend to have higher $\Sigma_{*,1\mathrm{kpc}}$ and lower $\mathrm{sSFR_{1kpc}}$ than star-forming galaxies in all redshifts.
6. Finally, we observe $\Sigma_{*,1\mathrm{kpc}}$–$\mathrm{sSFR_{in}}/\mathrm{sSFR_{out}}$ and M_*–$\mathrm{sSFR_{in}}/\mathrm{sSFR_{out}}$ relations with a negative slope, indicating that galaxies that are more massive and have a massive $\Sigma_{*,1\mathrm{kpc}}$ tend to have steeper sSFR suppression in their centers. The $\Sigma_{*,1\mathrm{kpc}}$–$\mathrm{sSFR_{in}}/\mathrm{sSFR_{out}}$ relation seems to be tighter than M_*–$\mathrm{sSFR_{in}}/\mathrm{sSFR_{out}}$ indicating that $\Sigma_{*,1\mathrm{kpc}}$ is more influential in driving $\mathrm{sSFR_{in}}/\mathrm{sSFR_{out}}$ than global M_*. The quiescent galaxies tend to have higher $\Sigma_{*,1\mathrm{kpc}}$ and $\mathrm{sSFR_{in}}/\mathrm{sSFR_{out}}<1$, suggesting that the formation of bulges might happen simultaneously with the quenching of star formation in the central regions.

Our work in this paper demonstrates the great potential of spatially resolved SED analysis using JWST imaging data. It is interesting to extend this study with larger-sample galaxies taken from various surveys to better understand the buildup of stellar mass in galaxies and the growth of their structures over cosmic time. More comprehensive comparisons with zoom-in cosmological simulations would help us to better understand the underlying physics. We will pursue this in our future work.

We thank the anonymous referee for providing valuable comments that helped to improve this paper. We thank Takahiro Morishita for the useful discussion and comments. This work is based on observations made with the NASA/ESA/CSA James Webb Space Telescope (JWST). Some of the data presented in this paper were obtained from the Mikulski Archive for Space Telescopes (MAST) at the Space Telescope Science Institute. The specific observations analyzed can be accessed via doi:10.17909/d2er-wq71 and doi:10.17909/cqfq-5n80. STScI is operated by the Association of Universities for Research in Astronomy, Inc., under NASA contract NAS526555. Support to MAST for these data is provided by the NASA Office of Space Science via grant NAG57584 and by other grants and contracts.

A. and T.H. are funded by a grant for JWST-GO-01433 provided by STScI under NASA contract NAS5-03127. The CosmicDawn Center is funded by the Danish National Research Foundation (DNRF) under grant #140. P.D. acknowledges support from the NWO grant 016.VIDI.189.162 ("ODIN") and from the European Commission's and University of Groningen's CO-FUND Rosalind Franklin program. R.A.W. acknowledges support from NASA JWST Interdisciplinary Scientist grants NAG5-12460, NNX14AN10G, and 80NSSC18K0200 from GSFC. A.Z. and A.K.M. acknowledge support by grant 2020750 from the United States–Israel Binational Science Foundation (BSF) and grant 2109066 from the United States National Science Foundation (NSF), and by the Ministry of Science & Technology, Israel. M.O. acknowledges support from JSPS KAKENHI grant Nos. JP22H01260, JP20H05856, JP20H00181, and JP22K21349. A.A. acknowledges support from the Swedish Research Council (Vetenskapsrådet project grants 2021-05559). E.V. acknowledges financial support through grants PRIN-MIUR 2017WSCC32, 2020SKSTHZ, and the INAF GO Grant 2022 (P.I. E. Vanzella).

Facilities: HST, JWST

Software: ASTROPY(Astropy Collaboration et al. 2013, 2018, 2022), PIXEDFIT (Abdurro'uf et al. 2021, 2022c), SEXTRACTOR (Bertin & Arnouts 1996), SEP (Barbary 2016), PHOTUTILS (Bradley et al. 2022a), GRIZLI (Brammer et al. 2022), EAZYPY (Brammer et al. 2008).

Appendix A
Robustness of the SED-fitting Method: Fitting Tests with Mock SEDs

To test the robustness of our SED-fitting method on this new set of photometric data, we perform SED-fitting tests using semiempirical mock SEDs, following a similar procedure as performed in Abdurro'uf et al. (2022a, Appendix A therein). We draw the parameter values for our mock SEDs from the measured parameters of real galaxies. In this case, we use the measured parameters obtained from our fitting to the SEDs within the central effective radius that were used for determining our photometric redshifts (see Section 3.5). Here, we use 290 galaxies selected randomly from 354 galaxies in the WHL 0137−08 (before further exclusion). We prefer to use the parameters of real galaxies to generate mock SEDs, instead of drawing them randomly because we cannot be sure that the combinations of those random parameters are physically

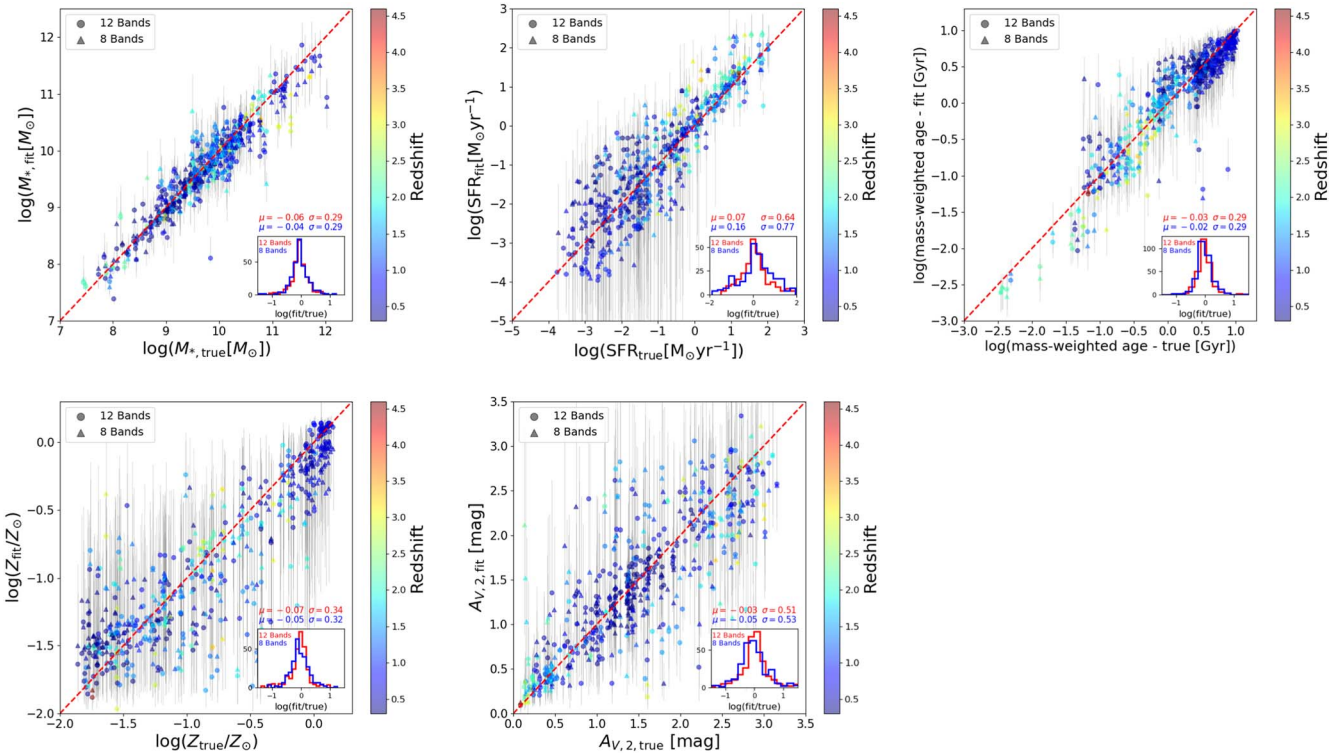

Figure 16. Comparisons between the best-fit parameters derived from SED-fitting tests using mock SEDs and the ground truth. In this test, two sets of photometry are used, one with a combined 12 filters of HST and JWST and the other with 8 filters of JWST. The results of those two SED-fitting tests are shown with different symbols (circles and triangles). Histograms in the insets show ratios between the best-fit parameters and the true values from the mock SEDs. The color coding of the data points represents redshift.

realistic. Using the set of parameters of 290 galaxies, we generate mock SEDs using the same modeling setup as in our main analysis. We generate two sets of mock SEDs: the first one with 12 filters of JWST and HST, the same set of filters as available for the WHL 0137−08 cluster, and the second set with 8 JWST filters, excluding HST filters. We then inject Gaussian noises assuming an S/N of 20 in all filters. After that, we fit the mock SEDs using the same method we used in the main analysis of this paper. For simplicity, here we fix the redshift.

We present the results in Figure 16, which shows the comparisons between the best-fit parameters derived from SED fitting and the true values from the mock SEDs. Histograms in the insets show ratios between the best-fit parameters and the true values. Results of the SED fitting with two sets of photometry are shown with different symbols and the histograms are shown with different colors. The data points are color coded based on their redshifts.

Overall, our SED fitting can recover the true parameters reasonably well. Stellar mass and mass-weighted age are recovered very well in both 8 band and 12 band SED fitting with small offset ($\lesssim$0.06 dex) and small standard deviation ($\lesssim$0.3 dex). It is interesting to see that the mass-weighed age is well recovered here. This may be due to the fact that our photometry covers the Balmer break and we have good photometry in rest-frame NIR from JWST, which also provides a good constraint for M_* (see Appendix B). The stellar metallicity (Z) and dust attenuation in the diffuse ISM ($A_{V,2}$) are also recovered well with an offset of $\lesssim$0.07 dex and a standard deviation of $\lesssim$0.5 dex although they look to be more scattered due to their small dynamical range. The SFR is more difficult to recover for passive galaxies (log(SFR) $\lesssim -1$) than for star-forming ones. For the whole sample, the SED fitting with 12 bands gives better SFR estimates (a small offset of 0.07 dex and a scatter of 0.64 dex) than with only JWST bands (offset of 0.16 dex and scatter of 0.77 dex).

Appendix B
The Age–Dust–Metallicity Degeneracy

The addition of JWST NIRCam data extends the wavelength coverage up to roughly the rest-frame NIR for our sample galaxies. This sufficiently wide wavelength coverage has the potential to break the well-known age–dust–metallicity degeneracy in SED fitting, which is very important for the analysis in this paper. In particular, it is crucial to be able to determine if the reddening observed in the central region of some galaxies in our sample is due to aging (i.e., quiescence) or dust attenuation. To check if our data set provides a sufficient constraint for resolving this degeneracy, we examine model color–color diagrams among the NIRCam filters. We base our analysis on the observed frame, instead of the rest frame, and explore different sets of filters for different redshifts. To generate model SEDs, we use an overall similar setting to that used in the main analysis of this paper and assume a double-power-law SFH with $\alpha = 3.0$, $\beta = 0.5$, and $\tau = 1.5$ Gyr, and $M_* = 10^{10.5} M_\odot$. We then generate model SEDs in grids of age, $A_{V,2}$, and metallicity. For simplicity, we assume $A_{V,1} = 1.5 \times A_{V,2}$.

Figure 17 shows the color–color diagrams of models at $z = 2.5$ and 3.5. Different colors represent different ages, whereas increasing marker size represents increasing metallicity (for the square symbol in the first column) and $A_{V,2}$ (for the circle symbol in the second column). For the two plots in the

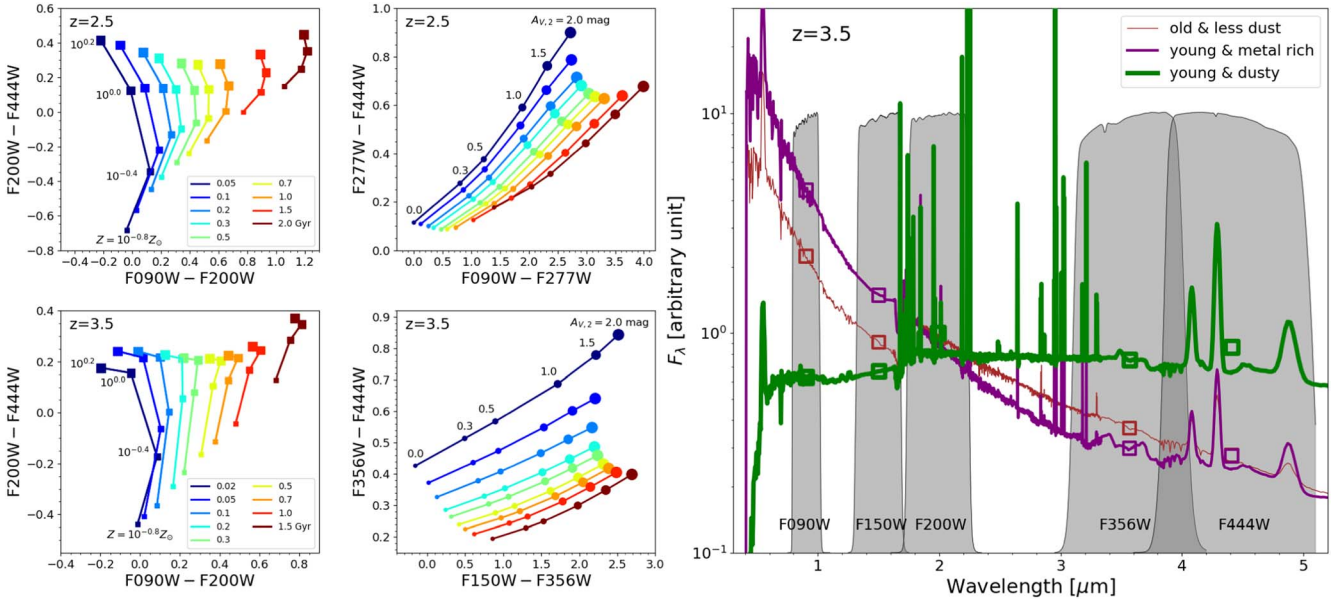

Figure 17. The patterns of model stellar populations on the observed-frame color–color diagrams involving JWST NIRCam filters. We plot the patterns of models at $z = 2.5$ and $z = 3.5$ on the color–color diagrams to check how good the NIRCam photometry is in resolving the degeneracies among age, dust attenuation, and metallicity in high redshifts. Different colors represent different ages, whereas increasing marker size represents increasing Z (for the square symbol) and increasing $A_{V,2}$ (for the circle symbol). The rightmost panel shows examples of the model SEDs of old less-dusty (brown color), young metal-rich (purple), and young dusty (green) galaxies at $z = 3.5$. The reddening effects by aging and dust are almost orthogonal with each other (i.e., distinguishable) on the F090W − F200W vs. F200W − F444W diagram. The reddening effects by aging and dust attenuation are distinguishable on the F090W − F277W vs. F277W − F444W diagram for $z = 2.5$ and the F150W − F356W vs. F356W − F444W diagram for $z = 3.5$.

first column, we fix $A_{V,2} = 0.0$, while for the two plots in the second column, we fix $Z = Z_\odot$. The F090W − F200W versus F200W − F444W diagram at the two redshifts seems to be able to distinguish the reddening effect by age and metallicity in such a way that both effects are almost orthogonal with each other. An increasing Z at a fixed age corresponds to reddening in F200W − F444W and roughly constant F090W − F200W (i.e., vertical shift on the diagram). On the other hand, increasing age tends to make reddening in the two colors (i.e., a diagonal shift on the diagram) for galaxies with low Z, while it corresponds to a roughly horizontal shift for galaxies with high Z.

In the second column, we show the relative effect of the dust attenuation and aging on F090W − F277W versus F277W − F444W (for $z = 2.5$) and F150W − F356W versus F356W − F444W (for $z = 3.5$) diagrams. The two effects are distinguishable in these two diagrams with dust attenuation and seem to make a diagonal shift, whereas an aging effect is roughly orthogonal to it. For an illustration, in the rightmost panel, we show examples of the model SEDs of old less-dusty (brown color; age1.5 Gyr, $\log(Z/Z_\odot) = -0.5$, $A_{V,2} = 0.1$ mag), young metal-rich (purple; age0.1 Gyr, $\log(Z/Z_\odot) = 0.2$, $A_{V,2} = 0.1$ mag), and young dusty (green; age0.1 Gyr, $\log(Z/Z_\odot) = -0.5$, $A_{V,2} = 2.0$ mag) galaxies $z = 3.5$. We normalize the SEDs by dividing them with the F200W flux. We also show the transmission curves of the filters that are used in the color–color diagrams for $z = 3.5$ in the left two columns. As we can see from this figure, the three model SEDs are distinguishable with NIRCam photometry. The reddening due to the dust attenuation is easily recognizable in the rest-frame UV to NIR, while that due to the metallicity is not easily recognizable in the rest-frame UV colors but it is detectable in the rest frame around the Balmer break (∼4000 Å) and NIR.

Appendix C
Construction of Empirical Point-spread Functions and Convolution Kernels

We generate the empirical PSFs of the HST ACS and JWST NIRcam filters in the WHL 0137−08 and MACS 0647+70 clusters by stacking images of bright isolated stars in those fields. For this, we use the PHOTUTILS package (Bradley et al. 2022a). We show the encircled energy of the empirical PSFs in the left column of Figure 18. After generating the PSFs, we then construct the convolution kernels that can be used for PSF matching. As described in Section 3.2, we perform PSF matching to homogenize the PSF sizes of our imaging data to match the PSF size of F444W, which is the largest among the filters used in our work. We also use PHOTUTILS to generate the kernels. To check the reliability of our kernels and PSF matching, we convolve the PSF images of the filters other than F444W with the kernels and compare the encircled energy of the convolved PSFs to that of the F444W filter. We show this comparison in the right column of Figure 18. As we can see from this figure, the convolved PSFs have similar encircled energy (with a small deviation of <0.1 dex around a radius of 0.″1), indicating the robustness of our PSF-matching process.

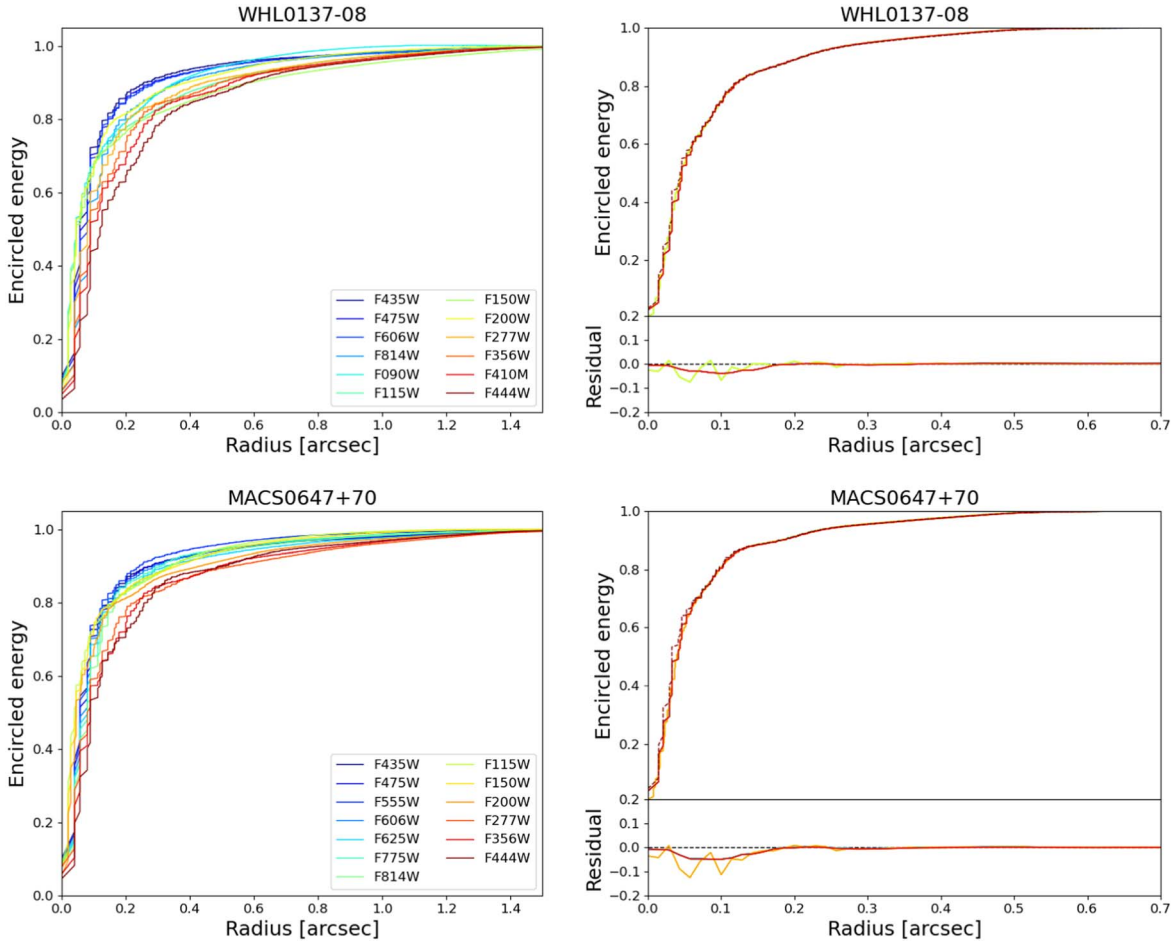

Figure 18. Left column: encircled energy of the empirical PSFs of the HST ACS and JWST NIRCam filters in the WHL 0137−08 and MACS 0647+70 clusters. The PSFs are generated by stacking the images of bright isolated stars in the fields. Right column: encircled energy of the PSFs after being convolved with kernels. The convolved PSFs have similar encircled energy, indicating the robustness of our PSF-matching process.

ORCID iDs

Abdurro'uf https://orcid.org/0000-0002-5258-8761
Dan Coe https://orcid.org/0000-0001-7410-7669
Intae Jung https://orcid.org/0000-0003-1187-4240
Henry C. Ferguson https://orcid.org/0000-0001-7113-2738
Gabriel Brammer https://orcid.org/0000-0003-2680-005X
Kartheik G. Iyer https://orcid.org/0000-0001-9298-3523
Larry D. Bradley https://orcid.org/0000-0002-7908-9284
Pratika Dayal https://orcid.org/0000-0001-8460-1564
Rogier A. Windhorst https://orcid.org/0000-0001-8156-6281
Adi Zitrin https://orcid.org/0000-0002-0350-4488
Ashish Kumar Meena https://orcid.org/0000-0002-7876-4321
Masamune Oguri https://orcid.org/0000-0003-3484-399X
Jose M. Diego https://orcid.org/0000-0001-9065-3926
Vasily Kokorev https://orcid.org/0000-0002-5588-9156
Paola Dimauro https://orcid.org/0000-0001-7399-2854
Angela Adamo https://orcid.org/0000-0002-8192-8091
Christopher J. Conselice https://orcid.org/0000-0003-1949-7638
Brian Welch https://orcid.org/0000-0003-1815-0114
Eros Vanzella https://orcid.org/0000-0002-5057-135X
Tiger Yu-Yang Hsiao https://orcid.org/0000-0003-4512-8705
Xinfeng Xu https://orcid.org/0000-0002-9217-7051
Namrata Roy https://orcid.org/0000-0002-4430-8846
Celia R. Mulcahey https://orcid.org/0000-0003-2434-2657

References

Abdurro'uf, & Akiyama, M. 2017, MNRAS, 469, 2806
Abdurro'uf, & Akiyama, M. 2018, MNRAS, 479, 5083
Abdurro'uf, Lin, Y.-T., Hirashita, H., et al. 2022a, ApJ, 926, 81
Abdurro'uf, Lin, Y.-T., Hirashita, H., et al. 2022b, ApJ, 935, 98
Abdurro'uf, Lin, Y.-T., Wu, P.-F., & Akiyama, M. 2021, ApJS, 254, 15
Abdurro'uf, Lin, Y.-T., Wu, P.-F., & Akiyama, M. 2022c, piXedfit: Analyze Spatially Resolved SEDs of Galaxies, Astrophysics Source Code Library, ascl: ascl:2207.033
Astropy Collaboration, Price-Whelan, A. M., Lim, P. L., et al. 2022, ApJ, 935, 167
Astropy Collaboration, Price-Whelan, A. M., Sipőcz, B. M., et al. 2018, AJ, 156, 123
Astropy Collaboration, Robitaille, T. P., Tollerud, E. J., et al. 2013, A&A, 558, A33
Aumer, M., & White, S. D. M. 2013, MNRAS, 428, 1055
Baker, W. M., Maiolino, R., Bluck, A. F. L., et al. 2022, MNRAS, 510, 3622
Barbary, K. 2016, JOSS, 1, 58
Barro, G., Faber, S. M., Koo, D. C., et al. 2017, ApJ, 840, 47
Bertin, E., & Arnouts, S. 1996, A&AS, 117, 393
Birnboim, Y., & Dekel, A. 2003, MNRAS, 345, 349
Bluck, A. F. L., Maiolino, R., Brownson, S., et al. 2022, A&A, 659, A160
Bluck, A. F. L., Maiolino, R., Piotrowska, J. M., et al. 2020, MNRAS, 499, 230
Bouché, N., Dekel, A., Genzel, R., et al. 2010, ApJ, 718, 1001

Boyer, M. L., Anderson, J., Gennaro, M., et al. 2022, RNAAS, 6, 191
Bradley, L., Sipőcz, B., Robitaille, T., et al. 2022a, astropy/photutils: v1.5.0, Zenodo, doi:10.5281/zenodo.6825092
Bradley, L. D., Coe, D., Brammer, G., et al. 2022b, arXiv:2210.01777
Brammer, G. 2022, Preliminary updates to the NIRCam photometric calibration, Zenodo, doi:10.5281/zenodo.7143382
Brammer, G., Strait, V., Matharu, J., & Momcheva, I. 2022, grizli, v1.5.0, Zenodo, doi:10.5281/zenodo.6672538
Brammer, G. B., van Dokkum, P. G., & Coppi, P. 2008, ApJ, 686, 1503
Brinchmann, J., Charlot, S., White, S. D. M., et al. 2004, MNRAS, 351, 1151
Broadhurst, T., Benítez, N., Coe, D., et al. 2005, ApJ, 621, 53
Bundy, K., Bershady, M. A., Law, D. R., et al. 2015, ApJ, 798, 7
Cano-Díaz, M., Sánchez, S. F., Zibetti, S., et al. 2016, ApJL, 821, L26
Casey, C. M., Zavala, J. A., Spilker, J., et al. 2018, ApJ, 862, 77
Cattaneo, A., Faber, S. M., Binney, J., et al. 2009, Natur, 460, 213
Ceverino, D., Klypin, A., Klimek, E. S., et al. 2014, MNRAS, 442, 1545
Chabrier, G. 2003, PASP, 115, 763
Chan, B. M. Y., Broadhurst, T., Lim, J., et al. 2017, ApJ, 835, 44
Charlot, S., & Fall, S. M. 2000, ApJ, 539, 718
Chen, C.-C., Gao, Z.-K., Hsu, Q.-N., et al. 2022, ApJL, 939, L7
Cheung, E., Faber, S. M., Koo, D. C., et al. 2012, ApJ, 760, 131
Ciotti, L., & Ostriker, J. P. 2007, ApJ, 665, 1038
Coe, D., Fuselier, E., Benítez, N., et al. 2008, ApJ, 681, 814
Coe, D., Salmon, B., Bradač, M., et al. 2019, ApJ, 884, 85
Coe, D., Umetsu, K., Zitrin, A., et al. 2012, ApJ, 757, 22
Coe, D., Zitrin, A., Carrasco, M., et al. 2013, ApJ, 762, 32
Cole, S., Lacey, C. G., Baugh, C. M., & Frenk, C. S. 2000, MNRAS, 319, 168
Conroy, C., & Gunn, J. E. 2010, ApJ, 712, 833
Conroy, C., Gunn, J. E., & White, M. 2009, ApJ, 699, 486
Croton, D. J., Springel, V., White, S. D. M., et al. 2006, MNRAS, 365, 11
Daddi, E., Bournaud, F., Walter, F., et al. 2010, ApJ, 713, 686
Daddi, E., Dickinson, M., Morrison, G., et al. 2007, ApJ, 670, 156
Dayal, P., & Ferrara, A. 2018, PhR, 780, 1
Dekel, A., & Birnboim, Y. 2006, MNRAS, 368, 2
Dekel, A., & Burkert, A. 2014, MNRAS, 438, 1870
Dekel, A., & Silk, J. 1986, ApJ, 303, 39
Di Matteo, T., Springel, V., & Hernquist, L. 2005, Natur, 433, 604
Diego, J. M., Protopapas, P., Sandvik, H. B., & Tegmark, M. 2005, MNRAS, 360, 477
Diego, J. M., Tegmark, M., Protopapas, P., & Sandvik, H. B. 2007, MNRAS, 375, 958
Dimauro, P., Daddi, E., Shankar, F., et al. 2022, MNRAS, 513, 256
Ebeling, H., Barrett, E., Donovan, D., et al. 2007, ApJL, 661, L33
Elbaz, D., Daddi, E., Le Borgne, D., et al. 2007, A&A, 468, 33
Ellison, S. L., Sánchez, S. F., Ibarra-Medel, H., et al. 2018, MNRAS, 474, 2039
Enia, A., Rodighiero, G., Morselli, L., et al. 2020, MNRAS, 493, 4107
Falcón-Barroso, J., Sánchez-Blázquez, P., Vazdekis, A., et al. 2011, A&A, 532, A95
Fang, J. J., Faber, S. M., Koo, D. C., & Dekel, A. 2013, ApJ, 776, 63
Ferland, G. J., Korista, K. T., Verner, D. A., et al. 1998, PASP, 110, 761
Ferland, G. J., Porter, R. L., van Hoof, P. A. M., et al. 2013, RMxAA, 49, 137
Ferreira, L., Adams, N., Conselice, C. J., et al. 2022, ApJL, 938, L2
Finkelstein, S. L., Bagley, M. B., Ferguson, H. C., et al. 2022, arXiv:2211.05792
Förster Schreiber, N. M., Renzini, A., Mancini, C., et al. 2018, ApJS, 238, 21
Fudamoto, Y., Oesch, P. A., Schouws, S., et al. 2021, Natur, 597, 489
Gaia Collaboration, Brown, A. G. A., Vallenari, A., et al. 2021, A&A, 649, A1
Genzel, R., Förster Schreiber, N. M., Lang, P., et al. 2014, ApJ, 785, 75
Genzel, R., Tacconi, L. J., Gracia-Carpio, J., et al. 2010, MNRAS, 407, 2091
Giménez-Arteaga, C., Oesch, P. A., Brammer, G. B., et al. 2022, arXiv:2212.08670
Girardi, L., Bressan, A., Bertelli, G., & Chiosi, C. 2000, A&AS, 141, 371
Häring, N., & Rix, H.-W. 2004, ApJL, 604, L89
Hoffmann, S. L., Mack, J., Avila, R., et al. 2021, AAS Meeting Abstracts, 53, 216.02
Hsiao, T. Y.-Y., Coe, D., Abdurro'uf, et al. 2022, arXiv:2210.14123
Hsieh, B. C., Lin, L., Lin, J. H., et al. 2017, ApJL, 851, L24
Inoue, A. K., Shimizu, I., Iwata, I., & Tanaka, M. 2014, MNRAS, 442, 1805
Iyer, K., Gawiser, E., Davé, R., et al. 2018, ApJ, 866, 120
Jullo, E., & Kneib, J. P. 2009, MNRAS, 395, 1319
Jullo, E., Kneib, J. P., Limousin, M., et al. 2007, NJPh, 9, 447
Jung, I., Finkelstein, S. L., Song, M., et al. 2017, ApJ, 834, 81
Kalita, B. S., Daddi, E., Bournaud, F., et al. 2022, A&A, 666, A44
Kartaltepe, J. S., Rose, C., Vanderhoof, B. N., et al. 2022, arXiv:2210.14713
Kereš, D., Katz, N., Fardal, M., Davé, R., & Weinberg, D. H. 2009, MNRAS, 395, 160
Kereš, D., Katz, N., Weinberg, D. H., & Davé, R. 2005, MNRAS, 363, 2
Kneib, J. P., Mellier, Y., Fort, B., & Mathez, G. 1993, A&A, 273, 367
Koekemoer, A. M., Fruchter, A. S., Hook, R. N., & Hack, W. 2003, HST Calibration Workshop : Hubble after the Installation of the ACS and the NICMOS Cooling System (Baltimore, MD: Space Telescope Science Institute), 337
Leja, J., Speagle, J. S., Ting, Y.-S., et al. 2022, ApJ, 936, 165
Leslie, S. K., Schinnerer, E., Liu, D., et al. 2020, ApJ, 899, 58
Lin, L., Pan, H.-A., Ellison, S. L., et al. 2019, ApJL, 884, L33
Madau, P., & Dickinson, M. 2014, ARA&A, 52, 415
Marigo, P., & Girardi, L. 2007, A&A, 469, 239
Marigo, P., Girardi, L., Bressan, A., et al. 2008, A&A, 482, 883
Martig, M., Bournaud, F., Teyssier, R., & Dekel, A. 2009, ApJ, 707, 250
McGreer, I. D., Mesinger, A., & D'Odorico, V. 2015, MNRAS, 447, 499
Meena, A. K., Zitrin, A., Jiménez-Teja, Y., et al. 2023, ApJL, 944, L6
Morishita, T., Ichikawa, T., & Kajisawa, M. 2014, ApJ, 785, 18
Morishita, T., Ichikawa, T., Noguchi, M., et al. 2015, ApJ, 805, 34
Morrissey, P., Conrow, T., Barlow, T. A., et al. 2007, ApJS, 173, 682
Morselli, L., Rodighiero, G., Enia, A., et al. 2020, MNRAS, 496, 4606
Murray, N., Quataert, E., & Thompson, T. A. 2005, ApJ, 618, 569
Nardiello, D., Bedin, L. R., Burgasser, A., et al. 2022, MNRAS, 517, 484
Nelson, E. J., van Dokkum, P. G., Brammer, G., et al. 2012, ApJL, 747, L28
Nelson, E. J., van Dokkum, P. G., Förster Schreiber, N. M., et al. 2016, ApJ, 828, 27
Nelson, E. J., Tacchella, S., Diemer, B., et al. 2021, MNRAS, 508, 219
Noeske, K. G., Weiner, B. J., Faber, S. M., et al. 2007, ApJL, 660, L43
Oguri, M. 2010, PASJ, 62, 1017
Pascale, M., Frye, B. L., Diego, J., et al. 2022, ApJL, 938, L6
Peng, C. Y., Ho, L. C., Impey, C. D., & Rix, H.-W. 2002, AJ, 124, 266
Pérez-González, P. G., Barro, G., Annunziatella, M., et al. 2022, arXiv:2211.00045
Popesso, P., Concas, A., Cresci, G., et al. 2023, MNRAS, 519, 1526
Postman, M., Coe, D., Benítez, N., et al. 2012, ApJS, 199, 25
Rieke, M. J., Kelly, D. M., Misselt, K., et al. 2022, arXiv:2212.12069
Rigby, J., Perrin, M., McElwain, M., et al. 2022, arXiv:2207.05632
Roberts-Borsani, G., Treu, T., Chen, W., et al. 2022, arXiv:2210.15639
Salmon, B., Papovich, C., Finkelstein, S. L., et al. 2015, ApJ, 799, 183
Sánchez, S. F. 2020, ARA&A, 58, 99
Sánchez, S. F., Rosales-Ortega, F. F., Jungwiert, B., et al. 2013, A&A, 554, A58
Sánchez-Blázquez, P., Peletier, R. F., Jiménez-Vicente, J., et al. 2006, MNRAS, 371, 703
Santini, P., Fontana, A., Castellano, M., et al. 2017, ApJ, 847, 76
Schutte, Z., Reines, A. E., & Greene, J. E. 2019, ApJ, 887, 245
Shen, S., Mo, H. J., White, S. D. M., et al. 2003, MNRAS, 343, 978
Skelton, R. E., Whitaker, K. E., Momcheva, I. G., et al. 2014, ApJS, 214, 24
Speagle, J. S., Steinhardt, C. L., Capak, P. L., & Silverman, J. D. 2014, ApJS, 214, 15
Suess, K. A., Kriek, M., Price, S. H., & Barro, G. 2019, ApJ, 877, 103
Tacchella, S., Carollo, C. M., Förster Schreiber, N. M., et al. 2018, ApJ, 859, 56
Tacchella, S., Carollo, C. M., Renzini, A., et al. 2015, Sci, 348, 314
Tacchella, S., Dekel, A., Carollo, C. M., et al. 2016a, MNRAS, 458, 242
Tacchella, S., Dekel, A., Carollo, C. M., et al. 2016b, MNRAS, 457, 2790
Tacchella, S., Forbes, J. C., & Caplar, N. 2020, MNRAS, 497, 698
Tadaki, K.-i., Genzel, R., Kodama, T., et al. 2017, ApJ, 834, 135
Tomczak, A. R., Quadri, R. F., Tran, K.-V. H., et al. 2016, ApJ, 817, 118
Treu, T., Schmidt, K. B., Trenti, M., Bradley, L. D., & Stiavelli, M. 2013, ApJL, 775, L29
van den Bosch, F. C. 2002, MNRAS, 332, 456
van der Wel, A., Franx, M., van Dokkum, P. G., et al. 2014, ApJ, 788, 28
van Dokkum, P. G., Leja, J., Nelson, E. J., et al. 2013, ApJL, 771, L35
van Dokkum, P. G., Nelson, E. J., Franx, M., et al. 2015, ApJ, 813, 23
van Dokkum, P. G., Whitaker, K. E., Brammer, G., et al. 2010, ApJ, 709, 1018
Vanzella, E., Claeyssens, A., Welch, B., et al. 2022, arXiv:2211.09839
Welch, B., Coe, D., Diego, J. M., et al. 2022a, Natur, 603, 815
Welch, B., Coe, D., Zackrisson, E., et al. 2022b, ApJ, 940, L1
Wen, Z. L., & Han, J. L. 2015, ApJ, 807, 178
Wen, Z. L., Han, J. L., & Liu, F. S. 2012, ApJS, 199, 34
Whitaker, K. E., Bezanson, R., van Dokkum, P. G., et al. 2017, ApJ, 838, 19

Whitaker, K. E., Franx, M., Leja, J., et al. 2014, ApJ, 795, 104
Whitaker, K. E., van Dokkum, P. G., Brammer, G., & Franx, M. 2012, ApJL, 754, L29
Williams, H., Kelly, P. L., Chen, W., et al. 2022, arXiv:2210.15699
Wuyts, S., Förster Schreiber, N. M., Nelson, E. J., et al. 2013, ApJ, 779, 135
Yang, L., Roberts-Borsani, G., Treu, T., et al. 2021, MNRAS, 501, 1028
York, D. G., Adelman, J., Anderson, J. E. J., et al. 2000, AJ, 120, 1579
Zitrin, A., Broadhurst, T., Barkana, R., Rephaeli, Y., & Benítez, N. 2011, MNRAS, 410, 1939
Zitrin, A., Broadhurst, T., Umetsu, K., et al. 2009, MNRAS, 396, 1985
Zitrin, A., Fabris, A., Merten, J., et al. 2015, ApJ, 801, 44
Zolotov, A., Dekel, A., Mandelker, N., et al. 2015, MNRAS, 450, 2327